Astronomy & Astrophysics manuscript no. Fornax_PNe
March 25, 2020

Fornax 3D project: automated detection of planetary nebulae in the centres of early-type galaxies and first results

T. W. Spriggs[1], M. Sarzi[1,2], R. Napiwotzki[1], P. M. Galán-de Anta[2,3], S. Viaene[1,5], B. Nedelchev[1], L. Coccato[8], E. M. Corsini[11,12], P. T. de Zeeuw[6,7], J. Falcón-Barroso[13,14], D. A. Gadotti[8], E. Iodice[4], M. Lyubenova[8], I. Martín-Navarro[9,10], R. M. McDermid[16], F. Pinna[13], G. van de Ven[17], and L. Zhu[10]

[1] Centre for Astrophysics Research, School of Physics, Astronomy and Mathematics, University of Hertfordshire, College Lane, Hatfield AL10 9AB, UK
[2] Armagh Observatory and Planetarium, College Hill, Armagh BT61 9DG, Northern Ireland, UK
[3] Astrophysics Research centre, School of Mathematics and Physics, Queen's University Belfast, Belfast BT7 INN, UK
[4] INAF–Osservatorio Astronomico di Capodimonte, via Moiariello 16, I-80131 Napoli, Italy
[5] Sterrenkundig Observatorium, Universiteit Gent, Krijgslaan 281, 9000 Gent, Belgium
[6] Sterrewacht Leiden, Leiden University, Postbus 9513, 2300 RA Leiden, The Netherlands
[7] Max-Planck-Institut fuer extraterrestrische Physik, Giessenbachstrasse, 85741 Garching bei Muenchen, Germany
[8] European Southern Observatory, Karl Schwarzschild Strasse 2, D-85748 Garching bei Muenchen, Germany
[9] University of California Observatories, 1156 High Street, Santa Cruz, CA 95064, USA
[10] Max-Planck-Institut fuer Astronomie, Koenigstuhl 17, D-69117 Heidelberg, Germany
[11] Dipartimento di Fisica e Astronomia 'G. Galilei', Università di Padova, vicolo dell'Osservatorio 3, I-35122 Padova, Italy
[12] INAF–Osservatorio Astronomico di Padova, vicolo dell'Osservatorio 5, I-35122 Padova, Italy
[13] Instituto de Astrofísica de Canarias, Vía Láctea s/n, E-38205 La Laguna, Tenerife, Spain
[14] Departamento de Astrofísica, Universidad de La Laguna, E-38205 La Laguna, Tenerife, Spain
[15] Ludwig Maximilian Universitaet, Professor-Huber-Platz 2, 80539 München, Germany
[16] Department of Physics and Astronomy, Macquarie University, Sydney, NSW 2109, Australia
[17] Department of Astrophysics, University of Vienna, Türkenschanzstrasse 17, 1180 Vienna, Austria

Received 07/10/2019; accepted 20/03/2020

ABSTRACT

Extragalactic Planetary Nebulae (PNe) are detectable via relatively strong nebulous [O III] emission, acting as direct probes into the local stellar population. Due to an apparently universal, invariant magnitude cut-off, PNe are also considered to be a remarkable standard candle for distance estimation. Through detecting PNe within the galaxies, we aim to connect the relative abundances of PNe to the properties of their host galaxy stellar population. By removing the stellar background components from FCC 167 and FCC 219, we aim to produce PN Luminosity Functions (PNLF) of those galaxies, and therefore also estimate the distance modulus to those two systems. Finally, we test the reliability and robustness of the our novel detection and analysis method. It detects the presence of unresolved point sources via their [O III] 5007Å emission, within regions previously unexplored. We model the [O III] emissions in both the spatial and spectral dimensions together, as afforded to us by the Multi Unit Spectroscopic Explorer (MUSE) and drawing on data gathered as part of the Fornax3D survey. For each source, we inspect the properties of the nebular emission lines present to remove other sources, that could hinder the safe construction of the PNLF, such as supernova remnants and H II regions. As a further step, we characterise any potential limitations and draw conclusions about the reliability of our modelling approach via a set of simulations. Through the application of this novel detection and modelling approach to Integral Field Unite (IFU) observations, we report for both galaxies: distance estimates, luminosity specific PNe frequency values. Furthermore, we include an overview into source contamination, galaxy differences and how they may affect the PNe populations in the dense stellar environments.

Key words. planetary nebulae: general – galaxies: elliptical and lenticular – cD galaxies: distances and redshift – techniques: imaging spectroscopy

1. Introduction

Planetary Nebulae (PNe) originate in a spectacular event occurring towards the end of the lifetime of most 2-8 $M_{\odot}$ stars, where copious amounts of oxygen rich stellar material is expelled outwards. The ejected material is subsequently ionised by UV radiation from the central star, with the forbidden [O III] 5007 Å line being prominent in many PNe, accompanied by the doublet line at 4959 Å. Planetary Nebulae thus act as isolated beacons within galaxies, allowing for their detection through spectroscopic observations (e.g. (Paczyński et al. 1971; Dopita et al. 1992)).

The study of extra-galactic PNe is centred around three major areas of research. The Planetary Nebular Luminosity Function (PNLF) as a viable distance indicator (Ciardullo et al. 1989). Furthermore, PNe can be used as direct probes of galaxy halo kinematics and dark matter content (Romanowsky et al. 2003; Douglas et al. 2007; Coccato et al. 2009; Kafle et al. 2018; Martin et al. 2018; Longobardi et al. 2018; Pulsoni et al. 2018; Bhattacharya et al. 2019a). Finally, PNe can be utilised to better understand the later stages of stellar evolution and in particular stellar environments different than the ones in our Galaxy (e.g. stellar metallicity and kinematics Marigo et al. 2004).

One of the more traditional techniques of detecting extragalactic PNe, with their radial velocity, is "on/off" band imaging, followed by spectroscopic measurements (either multi-slit or slit-less spectroscopy). Counter-dispersed slit-less spectroscopy, used for example in the Planetary Nebulae Spectrograph (Douglas et al. 2002, an instrument entirely dedicated to the study of extragalactic PNe), offer a better solution as it is capable of identifying and measuring position and velocity with a single observation, without follow-ups. In all these techniques, the identification of extra-galactic PNe is limited to the halo and outer regions of the host galaxy (typically > 0.5 effective radii, R_e), where the stellar continuum background does not dominate. As such, PNe have been detected within the intra-cluster mediums of the Comma and Hydra clusters (Gerhard et al. 2005; Ventimiglia et al. 2011), which reside at 100 Mpc and 50 Mpc respectively.

Previously, extragalactic surveys such as SAURON (Spectrographic Areal Unit for Research on Optical Nebulae) (Bacon et al. 2001) on the William Herschel Telescope (WHT), CALIFA (Calar Alto Legacy Integral Field Area) (Sanchez et al. 2011) on the Calar Alto Observatory (CAHA) telescope (Roth et al. 2005) and MaNGA (Mapping Nearby Galaxies at APO) (Bundy et al. 2014) on the Sloan Digital Sky Survey (SDSS) (York et al. 2000), have shown that modelling the background stellar continuum within galaxies is feasible and can be applied to a variety of data sets. This allows to cleanly isolate the ionised-gas emission in the galaxy spectra and to map the nebular activity across the entire field of view, including that originating from unresolved PNe sources. In this respect, the studies of Sarzi et al. (2011) and Pastorello et al. (2013) based on SAURON data for M32 and the central regions of Andromeda, illustrate well the ability of integral field spectroscopy to detect PNe down to the very central regions of external galaxies. With MUSE, the Multi Unit Spectroscopic Explorer (Bacon et al. 2010), we can detect PNe at even further distances, thanks in particular to its superior collecting power and spatial resolution. This was illustrated by Kreckel et al. (2017) in the case of the spiral galaxy NGC 628, at a distance of 9.6 Mpc. Then later, at twice the distance, in Sarzi et al. (2018), who presented preliminary results from one of the two Fornax cluster galaxies covered by the present study (FCC 167). Adaptive optics MUSE observations (e.g. Fahrion et al. (2019)) will certainly push the detections of extragalactic PNe even further.

With the detection of PNe by their prominent [O III] 5007 Å emissions, one can then start to investigate and catalogue their characteristics; total [O III] flux, apparent magnitudes, emission line ratios and line-of-sight velocities. Starting with the relative [O III] 5007Å apparent magnitude, the flux of a given PNe can be converted into a V-band corrected magnitude (Ciardullo et al. 1989, Eq. 1):

$$m_{5007} = -2.5 \log_{10}(F_{[\mathrm{O\,III}]}\ (\mathrm{erg\ cm^{-2}\ s^{-1}})) - 13.74. \quad (1)$$

Once sources of [O III] emissions have been identified and confirmed as PNe, we can then produce a PNLF for our detected sample and compare its shape to an empirically derived functional form of Ciardullo et al. (1989)'s PNLF, discussed later in Sect. 5. Estimating the PNLF is intrinsic to the process of using PNe as standard candle estimators. In extragalactic context, the PNLF has been shown to exhibit a cut-off value towards the bright end. Under the assumption that a universal PNLF holds true for all galaxies, and its brightest PNe are indeed detected, one can use the conversion of apparent into absolute magnitudes, to get an estimate for the distance to the host system. The steps of our analysis performing such an estimate are presented in Sect. 5. Another measurement the PNLF serves as a basis for, is the luminosity specific PN frequency, referred to as the α value. It is a proxy for the number of PNe expected to be produced per unit stellar luminosity of a particular galaxy.

Previous works have reported several interesting correlations of the halo α values and intrinsic host galaxy properties (Buzzoni et al. 2006; Coccato et al. 2009; Cortesi et al. 2013). Buzzoni et al. (2006) showed that α appears to be connected to the host galaxy's metallicity and UV excess. They found that as the host galaxy's core UV excess increased, the halo's α value decreased. A similar correlation was also found when core metallicity was compared to the halo's α value. It was interpreted to stem from the impacts metallicity has on stellar evolution and subsequent PNe formation. Further examples of reported correlations include the kinematics of the PNe system (parametrised either with the root mean square (rms) velocity (V_{rms}) or the shape of the velocity dispersion radial profile) with galaxy luminosity (optical and X-ray), angular momentum, isophotal shape parameter, total stellar mass, and the α parameter (Coccato et al. 2009).

Within this context, it is important to note that whereas our knowledge of both the shape and normalisation of the PNLF comes chiefly from peripheral PNe populations of galaxies, measurements for both the stellar metallicity and the UV spectral shape of the galaxies typically pertain to their central regions (well within one Re). For instance, in Buzzoni et al. (2006)'s study, they compare the properties of halo PNe populations with central measurements for the stellar kinematics, metallicity and UV excess. Integral-field spectroscopy (IFS) can overcome such a spatial inconsistency. Since IFS not only makes it possible to reveal PNe deeply in the central regions of galaxies, it also allows to measure the stellar age and metallicity in the same regions where the PNe are detected, including such regions as the stellar halos Weijmans et al. (first illustrated by 2009).

To progress along these lines, in this paper we illustrate how, with the aid of integral-field spectroscopy, we can characterise the PNe populations of external galaxies on the basis of the MUSE observations for two early-type galaxies in the Fornax cluster, namely FCC 167 (NGC 1380) and FCC 219 (NGC 1404). Excluding the central cluster galaxy NGC 1399, these are the two brightest objects inside the virial radius of the Fornax cluster, with a total r-band magnitude of $m_r = 9.3$ and 8.6, respectively (Iodice et al. 2019b). These ETGs are different, however, both morphologically and dynamically. FCC 167 is a fast-rotating S0a galaxy whereas FCC 219 is a slowly-rotating E2 galaxy with a kinematically decoupled core (Ricci et al. 2016, but see also Iodice et al. 2019a). Furthermore, FCC 219 is known to host a substantial hot-gas halo (e.g., Machacek et al. 2005) whereas FCC 167 shows a much weaker X-ray halo in the deep XMM-Newton images from Murakami et al. (2011) and Su et al. (2017), a difference that will be relevant to the discussion of our PNe results for these two objects. For this paper, we will initially assume a distance of 21.2 Mpc and 20.2 Mpc for FCC 167 and FCC 219, respectively, according to the surface-brightness fluctuation measurements of Blakeslee et al. (2009).

The paper is structured as follows; Section 2 details the data and targets from the Fornax 3D survey, along with a brief overview of the data analysis steps that aided our detection of PNe. Section 3 introduces our methodology regarding any of the PNe [O III] measurement and fitting processes, as well as the steps used in object identification. It also describes our PNe modelling simulations and our procedure for obtaining a sensible estimate of the instrumental Point Spread Function (PSF). In Section 4 we describe our results obtained by running our novel

1D+2D modelling approach, capable of the successful identification and extraction of the PNe populations of FCC 167 and FCC 219. Section 6 gives a brief overview of the PNLF and how incompleteness is accounted for. Finally, we compare our results with similar previous studies in Section 7 and present a discussion on the reasons for the potential tension in some of the available distance estimators and our estimates.

2. Observations and data reduction

FCC 167 and FCC 219 were observed with the MUSE integral-field spectroscopic unit (Bacon et al. 2010) as part of the magnitude-limited survey of galaxies within the virial radius of the Fornax galaxy cluster (Sarzi et al. 2018, hereafter Fornax3D). To cover both their central and outer regions (down to a surface-brightness limit of $\mu_B = 25$ mag arcsec^{-2}), Wide-Field-Mode, seeing limited, MUSE data were acquired over three and two separate pointings for FCC 167 and FCC 219, respectively, with total exposure times of 1h for central pointings and 1h30m for the intermediate or outer pointings. This provides high-quality spectroscopic measurements in $0.2'' \times 0.2''$ spatial elements over a 4650–9300Å wavelength range, with a spectral sampling of 1.25Å pixel^{-1}. As detailed in Sarzi et al., our MUSE data were reduced using the MUSE pipeline (Weilbacher et al. 2012, 2016) within the ESOREFLEX (Freudling et al. 2013) environment, where special care was taken in removing the sky background through the use of dedicated sky field exposures and of the Zürich Atmospheric Purge algorithm (Soto et al. 2016).

For the purpose of this paper, we obtained final datacubes for each pointing without further combining these into a single mosaic (as shown for instance in the case of FCC 167 in Sarzi et al. 2018). Indeed, to enable the study of galactic nuclei and unresolved sources, such as PNe and globular clusters, during the Fornax3D observations the central pointings had a stricter imaging requirement (FWHM $< 1.0''$) than the intermediate or outer pointings (FWHM $< 1.5''$). In that way, we use the data with highest MUSE quality in the regions where our pointings spatially overlap.

Finally, to ensure that the absolute flux calibration of our datacubes is correct, we applied to FCC 219 the same procedure, used in the case of FCC 167 in Sarzi et al. (2018), to compare with images obtained with the Hubble Space Telescope. Similarly, the MUSE flux densities for FCC 219 closely match those of HST

3. PNe sources identification and flux measurements

To compile a catalogue of PNe in our two target galaxies and measure their [O III] flux values we first proceed with a dedicated re-analysis of the MUSE datacubes (Sect. 3.1), then draw a conservative list of PNe candidate sources (Sect. 3.2) and finally fit (Sect. 3.3) and validate (Sect. 3.4) each PNe candidate with a 1D+2D model[1] that accounts for the expected, unresolved spatial distribution of the [O III] flux while optimising for the spectral position of the [O III] lines. A prior evaluation of the spatial point-spread function (PSF) is needed to inform this final fit (Sect. 3.5), which is done either by using foreground stars or by simultaneously applying our 1D+2D-model fitting approach to several bright PNe sources.

[1] GitHub/MUSE_PNe_fitting (Spriggs 2020)

3.1. Isolating the nebular emission component

To both identify and fit PNe sources we used pure emission-line datacubes, which are obtained after evaluating and subtracting the stellar continuum from each individual MUSE spectrum in our pointing datacubes. As detailed in Sarzi et al. (2018) and also shown in Viaene et al. (2019), this is done through a spaxel-by-spaxel simultaneous fit for both the stellar and ionised-gas spectrum using the GandALF (Sarzi et al. 2006) fitting tool, which in turn is informed by previous fits with both pPXF (Cappellari & Emsellem 2004; Cappellari 2017) and GandALF on Voronoi-binned spectra (Cappellari & Copin 2003), drawing on the IFU data-processing pipleline of Bittner et al. (GIST[2] 2019).

While emission-line cubes and other pipeline (stellar fitting) results are, in principle, available from this analysis (see also Iodice et al. 2019a), in the case of extended targets such as FCC 167 and FCC 219, we repeated our fitting procedure for individual MUSE pointing datacube. Furthermore, to achieve the best fit quality, and as described in Sarzi et al. (2018), the entire MILES (Sánchez-Blázquez et al. 2006) stellar library was utilised to match the stellar continuum rather than resorting to stellar population models (as shown in Fig. 5 of Sarzi et al. 2018). This is necessary to minimise stellar contamination, which could impact our scientific goals and improved the reliability of our nebular emission extraction.

3.2. PNe candidates identification

To obtain an initial list of PNe source candidates we draw from our spaxel-by-spaxel [O III] 5007 4959 ÅÅ line-fit results. Although our GandALF fits could already provide this information these are not properly optimised for the detection of PNe. We simply used GandALF to capture the general behaviour of any present ionised gas, including some regions of diffuse ionised-gas emission or active galactic nuclei activity. Those were safely identified and isolated from any potential unresolved PNe emission. When looking to locate PNe it is better to explicitly account for the fact that PNe have only modest expansion velocities (between 10 and 40 km s^{-1}; Weinberger et al. 1983; Hajian et al. 2007; Schönberner et al. 2014) leading to [O III] line profiles that should be near the instrumental resolution limit. For this reason, we re-fit for the [O III] 4959 and 5007 ÅÅdoublet in only the 4900 – 5100 Å spectral region of our pure emission-line cubes. Here, we are assuming a constant intrinsic stellar velocity dispersion for the PN (see Sect. 3.4 below for values) and an instrumental spectral resolution ($\sigma_{\rm MUSE,LSF}$) at 5007Å of 75 km s^{-1} according to the MUSE line-spread function (LSF) behaviour, measured by Guérou et al. (2017).

The results of this dedicated [O III] doublet fit and its ability to reveal the presence of unresolved [O III] sources is shown in Figs. 1 and 2 for FCC 167 and FCC 219, respectively. In particular, these maps show the value for the ratio of the fitted peak amplitude of the [O III] 5007 line (A) and the residual-noise level (rN) from our fits around the [O III] doublet. The residual noise level was evaluated as the standard deviation of the residuals after subtracting our [O III] model from the data. As discussed in Sarzi et al. (2006), this A/rN ratio is a good measure for the threshold beyond which emission lines can be detected and for how well they can be measured. Therefore, such A/rN maps provide a better contrast between [O III] sources and regions dominated by false-positive [O III] detection, in comparison to maps of either line amplitudes or fluxes.

[2] https://abittner.gitlab.io/thegistpipeline

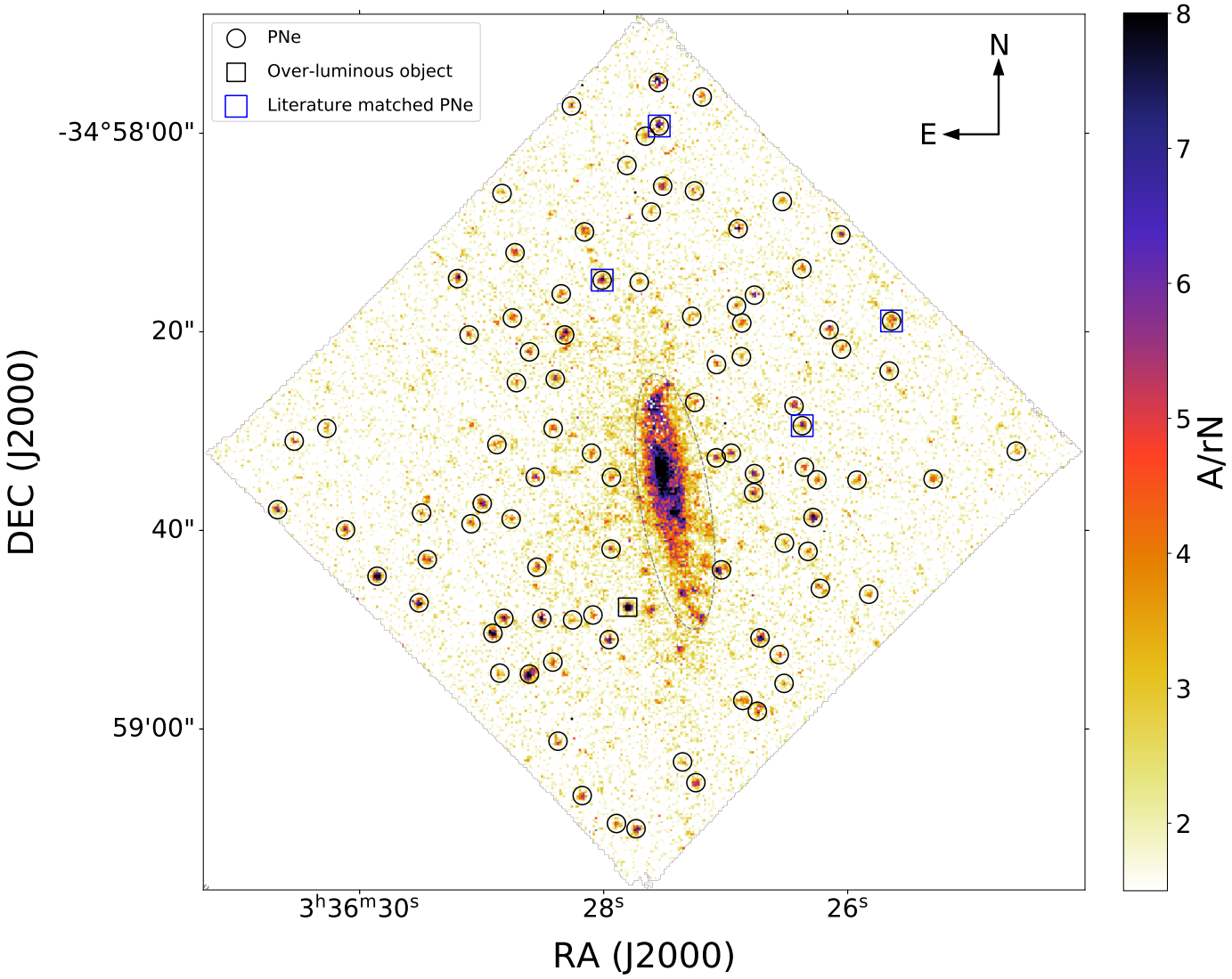

Fig. 1. FCC 167: Map of the peak amplitude to residual-noise level ratio (A/rN) of the [O III]5007 line, based on our spaxel-by-spaxel fit for the [O III] doublet in the emission datacube. The sources detected and labelled PNe, are shown by a black circle. The over-luminous object (see Sect. 5.1) is highlighted by a black square. The PNe matched with those reported by Feldmeier et al. (2007) are highlighted by blue squares. The dashed ellipsoid marks the central region that was disregarded owing to the presence of diffuse ionised-gas emission (see also Viaene et al. 2019).

With these signal-to-noise (A/rN) maps at hand, we compiled an initial list of PNe candidates using the Python package SEP, a python script-able version of the popular Sextractor source-finding routine of Bertin & Arnouts (1996). First, a background noise evaluation is carried out, and the subsequent noise map is subtracted from the A/rN data. Having first tested this approach against a no-background-subtraction attempt, that also used a larger central exclusion region, we concluded that subtracting the SEP derived background aided in avoiding spurious sources, and meant that the masked region could be much smaller than before. We adopted a rather conservative source-detection threshold corresponding to two standard deviations above the SEP derived, background noise. This decision proved to strike the balance between detecting an excessive number of sources, that would result in a larger fraction subsequent of source exclusions, versus detecting the more prominent sources that would make up the majority of the validated PNe. Figures 1 and 2 highlight the sources that are present within the field of view (FOV), with excluded sources circled in red. The dashed line regions are excluded due to known diffuse ionised-gas emission (e.g., for FCC 167 in Fig. 1, see also Viaene et al. 2019), or contain regions where template-mismatch was found to bias our flux measurements (e.g. seen in FCC 219, in Fig. 2).

3.3. Candidate PNe Fitting

To validate the unresolved nature of our PNe candidates and measure their kinematics and total [O III] 5007Å fluxes, we started by fitting each of them with a procedure that used all the information contained in the emission-line cube, near the spatial location of the source (in a 9×9 spaxel region that is 1.8″across) and in the wavelength region around the [O III] doublet (between 4900 Å and 5100 Å). Specifically, we simultaneously match all the MUSE spectra in such a portion of our emission-line cube with a 1D+2D emission-line model where the total [O III] 5007Å flux ($F_{[\mathrm{O\,III}]}$) of the model, the shape of the PSF, and the exact spatial positioning of the model determines the [O III] model flux

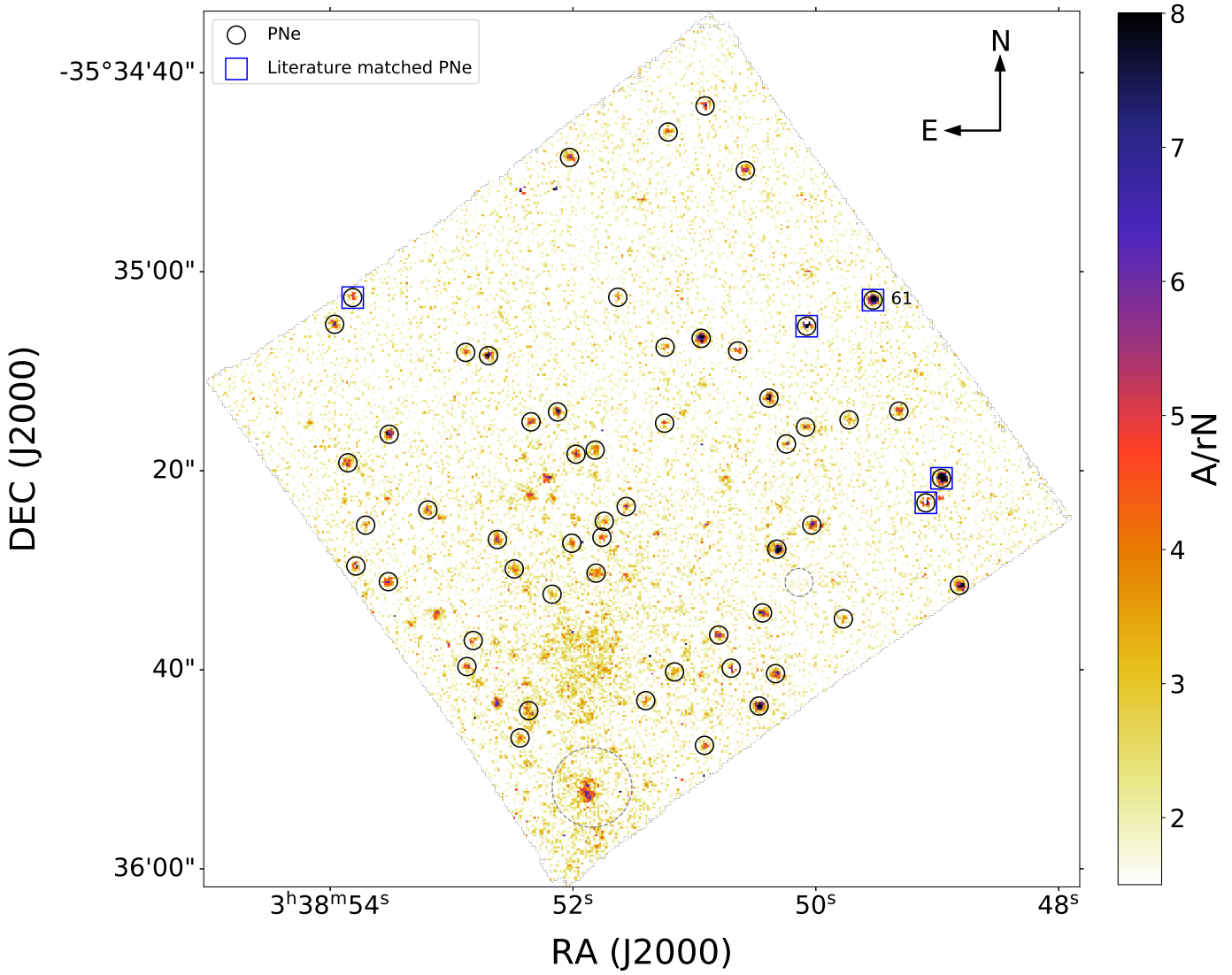

Fig. 2. FCC 219: Similar to Fig.1 but showcasing the PNe within FCC 219. Sources are highlighted by black circles, along with blue squares indicating the sources that we matched with McMillan et al. (1993) within the field of view.
The central mask, located towards the south of the FOV (dashed circle), excludes regions affected by diffuse ionised-gas emission (see Iodice et al. 2019a). There is also a foreground star masked out, indicated by a small dashed circle, located towards the right of the FOV.

at each spaxel ($F_{[\mathrm{O\,III}]}(x, y)$). This in turn can be translated into a model [O III] 5007 4959 ÅÅ line profile through our knowledge of instrumental LSF and the optimisation of the PN's emission intrinsic width σ_{PNe} and velocity v (although in practise we solve for the total profile width σ_{tot}, which incorporates the convolution of both the LSF and σ_{PNe}).

Assuming a Moffat (1969) profile for the PSF, the [O III] 5007Å flux distribution around a PNe source can be written as

$$F_{[\mathrm{O\,III}]}(x, y) = F_{[\mathrm{O\,III}]}(x_0, y_0) \left(1 + \frac{(x - x_0)^2 + (y - y_0)^2}{\alpha^2}\right)^{-\beta}, \quad (2)$$

where α and β determine the radial extent and kurtosis of the Moffat distribution, x_0 and y_0 locate the source centre and $F_{[\mathrm{O\,III}]}(x_0, y_0)$ is the peak [O III] flux at this position. The latter is related to total [O III] flux through the Moffat profile normalisation

$$F_{[\mathrm{O\,III}]}(x_0, y_0) = F_{[\mathrm{O\,III}]} \frac{\beta - 1}{\pi\alpha^2}. \quad (3)$$

The spatial extent of our sources can also be quantified using the full-width at half maximum of the Moffat profile that is given by

$$\mathrm{FWHM} = 2\alpha\sqrt{2^{1/\beta} - 1}. \quad (4)$$

In its more general form, therefore, this model includes seven free parameters ($F_{[\mathrm{O\,III}]}, v, \sigma_{\mathrm{total}}, x_0, y_0$ for the PN source, α and β for the PSF) plus two additional parameters to account for background remaining after the continuum subtraction (spectrum background level and gradient). These parameters are all optimised through a standard non-linear χ^2 minimisation (Newville et al. 2014, 2019). In practice, however, the full set of parameters are only varied initially, when constraining the PSF of our observations or to estimate the typical value of σ_{tot} (Sect. 3.5). Once both the values of σ_{tot} and the PSF are determined, we hold σ_{tot}, α, and β fixed, allowing for the rest of the parameters to vary.

Figure 3 illustrates the working of our 1D+2D-fitting, in the case of a PN source (61) in the central region of FCC 219

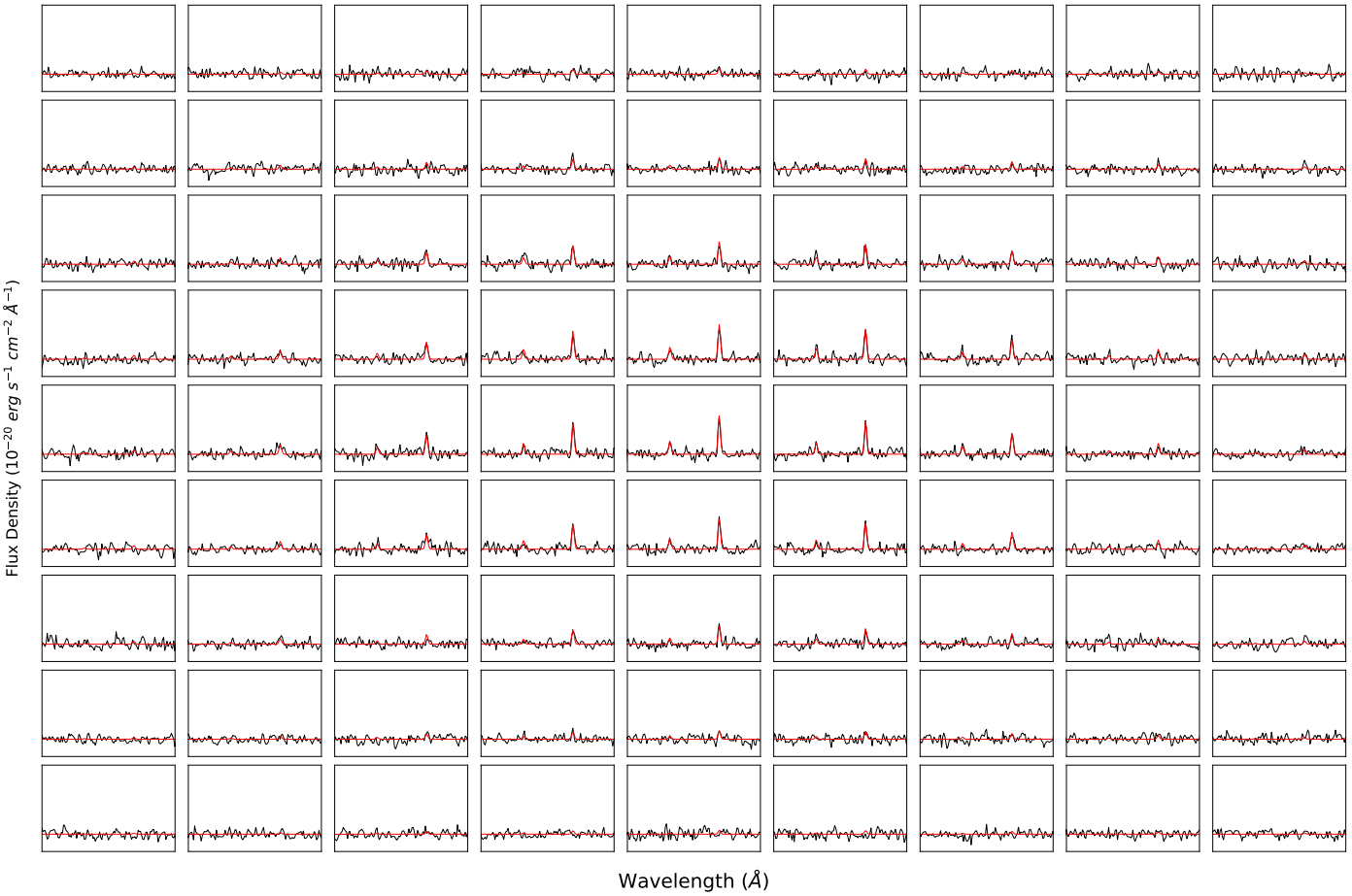

Fig. 3. Example of an outcome from our 3D fitting for one PNe source (61), located in the central region of FCC 219 (see Fig. 2). For each of the 9 × 9 spaxels plotted, the corresponding wavelength range spans 4950-5080 Å. The scale of the y-axis is chosen arbitrarily to best illustrate our fits. Spectral data is shown in black, with our [O III] doublet model shown in red. The entire 9x9 spaxel region is displayed to reinforce the expected variation in signal (central pixels) and noise (outer pixels). Each spaxel corresponds to a spatial scale of 0.2 arcsecond.

(Fig. 2). In particular, by imposing a PSF behaviour to the intensity of the model profile for the [O III] doublet at each spaxel position around the candidate PN, our approach automatically checks the unresolved nature of the emission-line source while minimising any bias on the recovered parameters that could be potentially introduced by regions with little or no [O III] flux. Furthermore, by also considering the spectral component of the data, this technique allows us to isolate PNe embedded in diffuse ionised gas components, as well as distinguish two blended PNe sources with different kinematics (see, e.g., Pastorello et al. 2013). Last, but not least, thanks to the ubiquity of PNe this method also offers a way to measure the PSF when targeting galaxies with IFS observations.

3.4. PNe candidate validation

Once our initial 1D+2D fits were at hand, we could further filter objects that do not show typical PNe characteristics. Those include detections not consistent with unresolved sources, in which our fit results could be either biased by the presence of broader ionised-gas emission or have a fair chance of being the consequence of a false-positive detection.

To check that the [O III] flux distribution of our candidate source is consistent with a given PSF, we rely on the quality of our fits. Therefore, we exclude objects where the χ^2 value returned by our fit is outside the 95 percent confidence limit for a χ^2 distribution with ν degrees of freedom (corresponding to $9 \times 9 \times N_\lambda$ data points, minus the six free parameters).

To understand when our fit results can be deemed reliable, we run a set of simulations, in particular, to pin-point when the recovery of key parameters becomes biased in the low signal-to-noise regime. For this, we created a number of mock PNe data in the same kind of emission-line 9×9 minicubes that are passed to our 1D+2D-fitter, with total $F_{[\mathrm{O\,III}]}$ values corresponding to PNe over a range of absolute M_{5007} magnitudes (between -4.5 and -1.0 in steps of 0.05), observed at the estimated D_{PNLF} in FCC 167 (see Sect. 7). These emission lines were spatially distributed according to the measured PSF of our central observations, with the peak of the emissions located at towards the centre of the minicube. The local [O III] flux at each spaxel is then converted into an [O III] doublet profile for a PNe moving at the systemic velocity of FCC 167 (1878 kms^{-1} Iodice et al. (2019a)), The [O III] profile width was set to the value of $\sigma_{\mathrm{tot}} \sim 200$ km s^{-1}, as found from the PSF fitting (Sect. 3.5), which corresponds to an intrinsic line broadening (σ_{PNe} of 40km s^{-1}), considering the value of the MUSE LSF ($\sigma_{\mathrm{MUSE,LSF}}$). Finally, random Gaussian noise was added to a level typical of the fit-residual noise (rN) found in the central pointing of FCC 167 (located outside the masked region of Fig.1, predominantly containing diffuse ionised-gas emission). Such a simulation set-up allows us to explore how well our 1D+2D-fitting approach recovers the simulated PNe's total flux, flux distribution and kinematics, at differ-

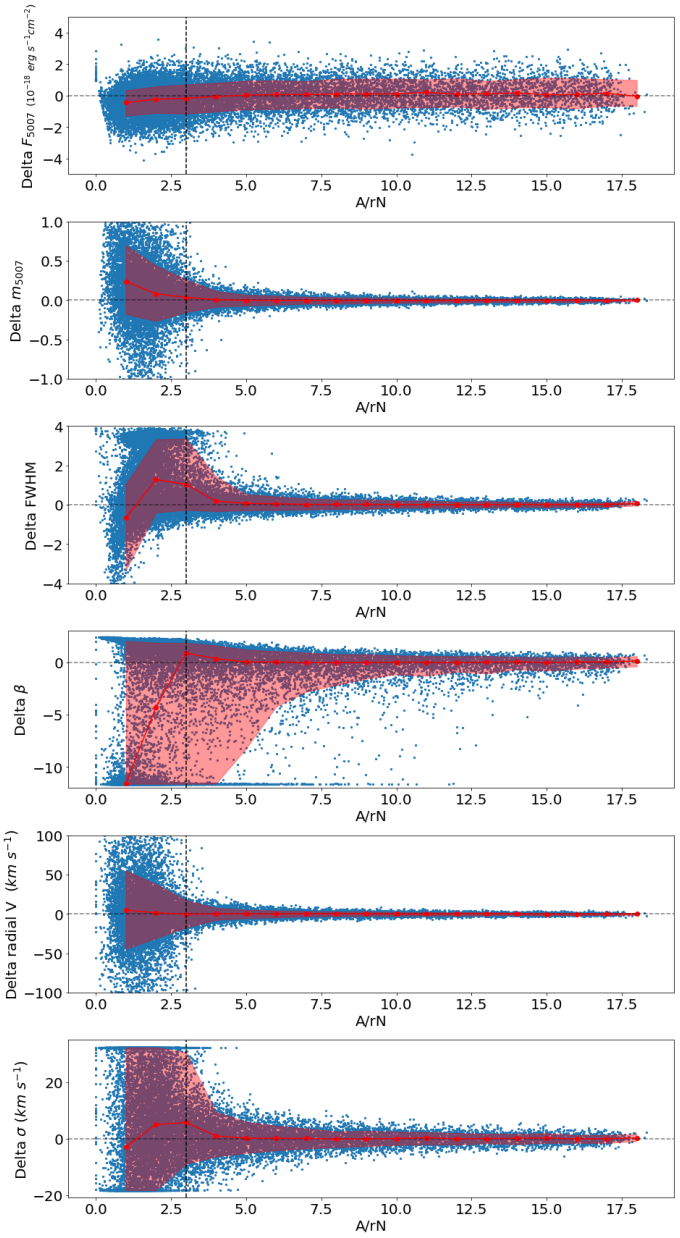

Fig. 4. Simulating the detection and retrieval of PSF parameters FWHM and β, as well as determining how accurately the model fits for the total flux of a source. The blue points are the individual simulation results, the red points are the median values, binned in A/rN, with the upper and lower regions of the red region indicating the 86th and 16th percentile respectively. Top/First: delta [O III] flux, second: delta M_{5007}, third: delta FWHM, fourth: delta β, fifth: delta radial velocity derived from wavelength position, and sixth: delta velocity dispersion of the [O III] emission lines.

ent levels of background-noise contamination. To quantify the latter, we consider the ratio between the maximum [O III] 5007 line amplitude at the centre of our model and the residual noise level (rN).

The [O III] profile width was set to the value of $\sigma_{\rm tot} \sim 200\,{\rm km\,s^{-1}}$, as found from the PSF fitting (Sect. 3.5), which corresponds to an intrinsic line broadening ($\sigma_{\rm PNe}$ of $40\,{\rm km\,s^{-1}}$), considering the value of the MUSE LSF ($\sigma_{\rm MUSE,LSF}$).

$$\sigma_{tot} = \sqrt{\sigma^2_{MUSE,LSF} + \sigma^2_{PNe}}. \quad (5)$$

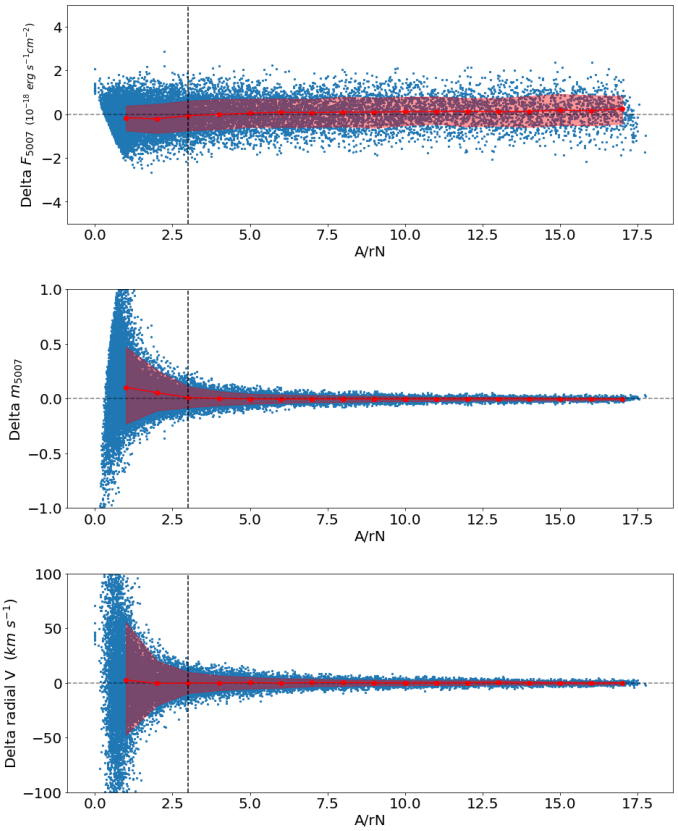

Fig. 5. Simulation results when the PSF values of FWHM and β are known and held constant. Top: Delta Flux of [O III] against fitted A/rN value of each source. Middle: Delta M_{5007} against source A/rN. Bottom: Delta radial velocity as measured from the offset of the [O III] emission line. The red points are the median value binned by A/rN, with the 16th and 84th percentile range indicated by the filled red regions.

$$A_{[\rm O\,III]}(x_0, y_0) = \frac{F_{[\rm O\,III]}(x_0, y_0)}{\sqrt{2\pi}\,\sigma_{tot}}. \quad (6)$$

Starting with the most general case (i.e. trying to recover all parameters), Fig. 4 shows not only how the accuracy of the recovered parameters decreases at lower central A/rN values, but also highlights parameters that are biased towards the lower signal-to-noise regime. These biases appear most pronounced in the PSF parameters, notably below five A/rN, along with the estimation of the PN's [o III] emission velocity dispersion σ_{tot}. Although these biases only have a limited knock-on effect on the measured total flux, at low A/rN values the uncertainties in the absolute M_{5007} magnitudes quickly reach values that can impact the distance estimates (e.g., a 0.2 magnitude error implies a 10 percent error on any attempted distance estimates based on the PNLF).

As mentioned above, whereas Fig. 4 has some relevance for our PSF determination (see Sect. 3.5) we typically measure our PNe candidate sources while holding to the best fit PSF parameters and value of σ derived from bright PNe or stars in the field. Under these conditions the behaviour of our 1D+2D-fitting approach is shown by Fig. 5, through which we can conclude that above a central $A/rN = 3$ the recovered absolute magnitude values are essentially unbiased and accurate to 0.1 magnitude or below.

To complement these idealised simulations, we also assess the level of false-positive contamination by running our 1D+2D-

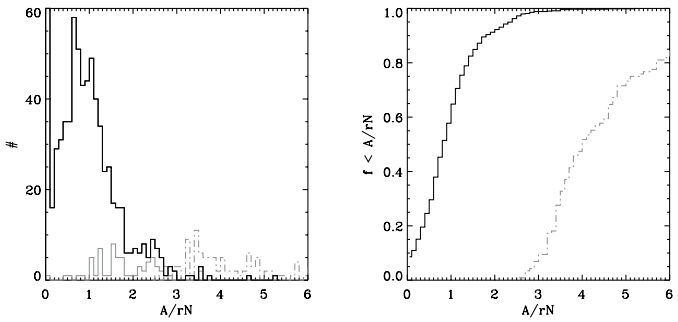

Fig. 6. Central A/rN values from 1D+2D-fits to regions devoid of emission in FCC 167. Left: observed false-positive A/rN values distribution. The grey line shows the values corresponding to regions closer to the centre, where template-mismatch in the emission-line cube systematically bias the A/rN values to higher values. For comparison, the dot-dashed grey lines show also the distribution of A/rN values for our candidate sources. Right: cumulative distribution for the false-positive A/rN values. 99% of these lie below A/rN=3. A/rN values corresponding to poor fits are excluded.

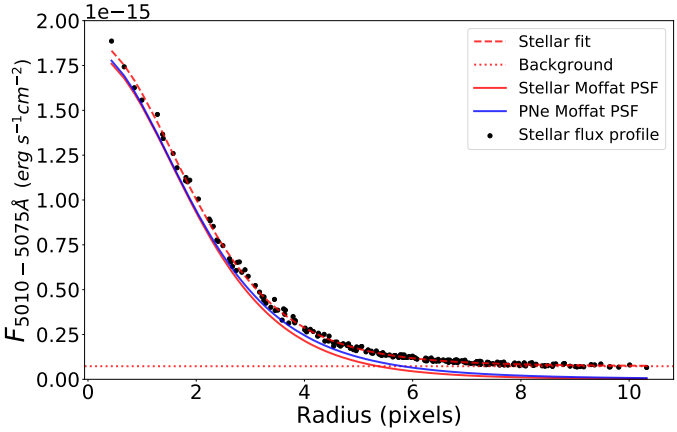

Fig. 7. The radial profile of the star within the FOV of FCC 219 (black dots). The best-fit model to the stellar light is shown by the red dashed line, with the red dotted line indicating the background level of galaxy light. The solid red and blue lines depict the actual PSF, without background, as described by the star and PNe, respectively. In regards to the total flux and profile, this comparison highlights the close agreement between the two approaches.

fitting code at randomly-selected locations. In this procedure, we excluded regions with known diffuse ionised-gas emission, as well as the locations of our candidate PNe sources. Figure 6 shows the distribution for the central A/rN values obtained from fits to noise, for FCC 167, indicating that 99 percent of the amplitude of such false positives ($A_{\rm false\ pos}$) results lie below three times the residual noise ($A_{\rm false\ pos}/rN < 3$). The grey lines in Fig. 6 illustrates the results of fitting sources closer to the central, masked regions of the galaxy, due to the higher complexity and density of stellar light. Here, template mismatch produces erroneous [O III] signal, i.e. increased background levels which cause the fitter to mistake spectral noise for [O III] emission lines. This then produces higher $A_{\rm false\ pos}/rN$ values, with a greater fraction of $A_{\rm false\ pos}/rN$ above our imposed cut off of three times the residual noise.

In summary, we validate our PNe candidate sources using standard χ^2 statistic to check the quality of our 1D+2D fits and consider only objects where the central $A/rN > 3$, all the while excluding regions with diffuse ionised-gas emission or where template mismatch can lead to false-positive detection with central A/rN above this threshold.

3.5. Point spread function determination

An accurate knowledge of the PSF is key to our PNe flux measurements. A Moffat (1969) profile (Eq. 2) generally describes well the PSF of astronomical observations, including those obtained with MUSE (Bacon et al. 2010).

To measure the PSF from our MUSE data we relied either on foreground stars in the field-of-view of our MUSE pointing or on the PNe sources themselves when no star was available. To deal with both situations, on the one hand, we modified our 1D+2D-fitting code allowing to ignore the spectral direction and thus fit the flux distribution of a star, and on the other hand implemented the option to fit several PNe sources at the same time. In the latter case we hold to the same PSF parameters α and β as well as to a common intrinsic $\sigma_{\rm tot}$ across the different sources, while individually optimising only for $F_{\rm [O\,III]}, v, x_0, y_0$ as well as for the two continuum-shape nuisance parameters: gradient and background level. Typically, we found that up to 10 of the better detected PNe during this process were enough to consider. These PNe were with central A/rN values of at least eight as estimated from an initial 1D+2D-fit with all parameters free to achieve a satisfactory estimate for the PSF. When constraining the PSF from foreground stars, we also allowed for a constant flux background from the host galaxy.

Table 1. Best estimates for the Moffat PSF parameters in our target galaxies, as derived using either foreground stars or PNe. The corresponding FWHM of our Moffat models are also compared to the FWHM measurements from the MUSE data header, as obtained by the MUSE slow guiding system.

Galaxy	Method	α	β	FWHM (pixels)	$\rm FWHM_{HDR}$ (pixels)
FCC 167	PNe	2.99	2.15	3.69	3.56
FCC 219	PNe	4.26	3.37	4.07	3.50
FCC 219	Star	4.29	3.42	4.07	3.50

To illustrate the accuracy with which the PSF is measured using PNe sources, in Fig. 7 we show the surface-brightness profile for the foreground south-western star in the field-of-view of central pointing of FCC 219 and the associated star best-fitting Moffat model. We note that it compares rather well to the best-fitting Moffat profile as extracted from PNe. This is further quantified in Table 1, where we compare our PSF estimation with the one provided by the MUSE cube, as determined on the basis of a fit to the galaxy itself. Typical errors in the PSF parameters translate into total PSF flux uncertainties of less than nine percent. In particular, with such accuracy for the PSF, we could set a limit of potential systematic error on our PNe magnitude estimates of less than 0.1 mag.

To conclude, we note that even if a star is present, we would run our simultaneous PNe procedure in order to constrain the typical σ_{tot} of the PNe in the target galaxy.

3.6. Literature comparison

To date, the most comprehensive PNe cataloguing for both FCC 167 and FCC 219 were compiled by Feldmeier et al. (2007) and McMillan et al. (1993), respectively. The PNe detection method used in these surveys is the "on-off" photometry, as as

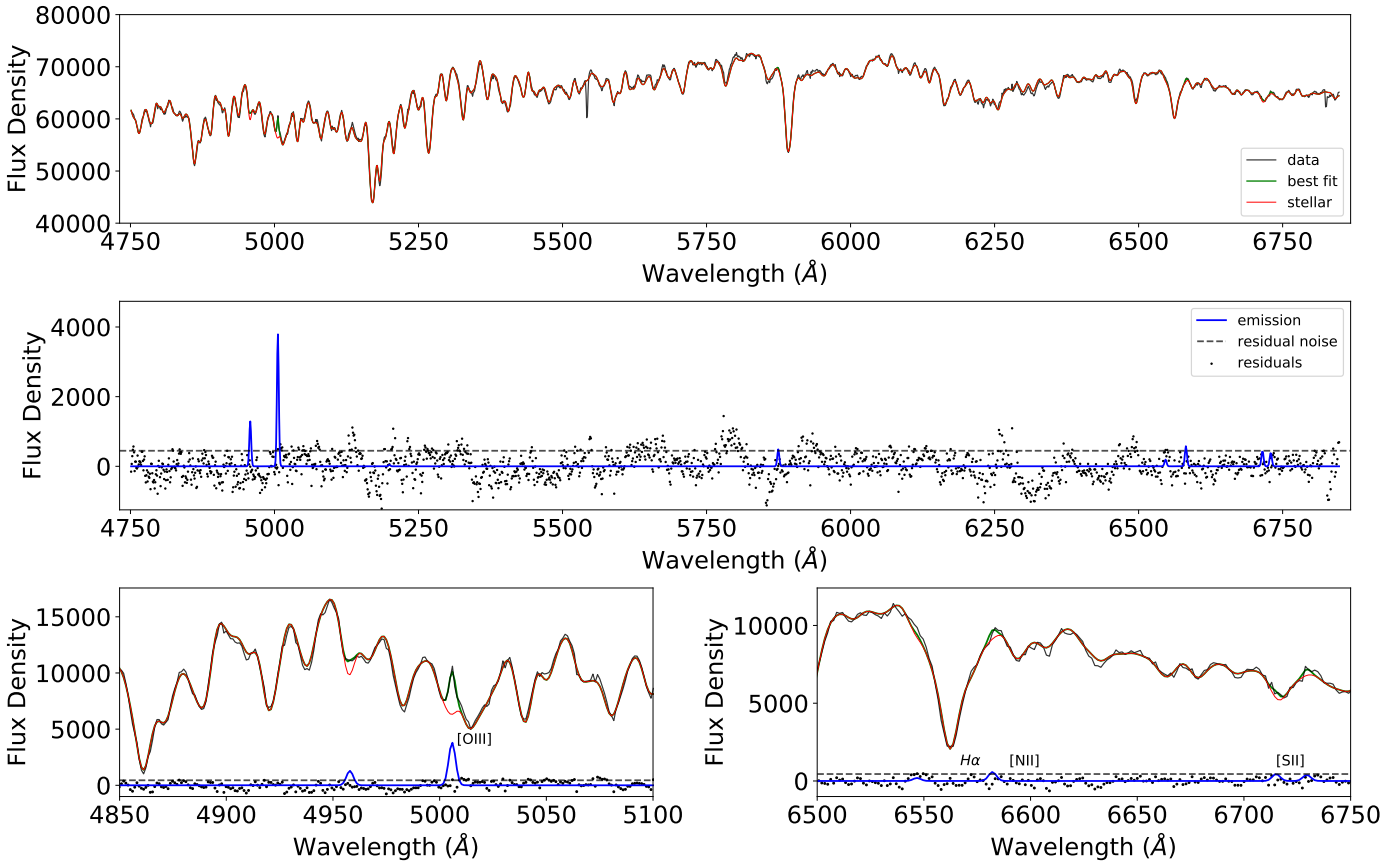

Fig. 8. GandALF fit to the typical spectrum (green) of a PNe source (black line, top plot), from FCC 167 (F3D J033627.08-345832.69), and its galaxy stellar background (red), showing strong [O III] lines and some Hα emission. The middle plot shows the emission lines as detected by GandALF (blue), with the dashed, horizontal line indicating the level of residual noise (standard deviation of the residuals from stellar subtraction (black points)). The lower left panel zooms in the Hβ and [O III] doublet wavelength region, whereas the lower right panel shows the region occupied by Hα and the [N II] and [S II] doublets. The data, best fit and stellar spectra shown in the bottom two plots are subtracted by an arbitrary number to better present and compare the fit of the nebulous and stellar emissions, within each region.

such these studies find PNe mostly in the galaxy outskirts. We are however, able to match a select few sources located towards the edges of our central observations as well as in the outer pointings of each galaxy.

Within the central and disk pointings of FCC167, we match 21 PNe with the records of Feldmeier et al. (2007), the majority of which are located outside of our central pointing. From comparing their catalogue, we conclude that we do not miss any PNe within our FOV. After comparing the measured magnitudes, we find a linear agreement seen in Fig.10; see Sect. 5.3, though with a systematic offset of 0.45 mag fainter than their recorded values. The origin of such an offset is unclear. We are confident in our own flux calibration, which is based on HST images, and further note that Feldmeier's brighter m_{5007} values lead to a rather small distance modulus for FCC167: $31.04^{+0.11}_{-0.15}$ (16.1 Mpc).

For FCC219, McMillan et al. (1993) find nine PNe sources within the regions we mapped. One of their sources is excluded within our catalogue due to being filtered out. Fig. 11 shows the scatter of McMillan's m_{5007} values versus those presented here. We also note that McMillan et al. (1993) report a distance modulus of $31.15^{+0.07}_{-0.1}$ (17.0 Mpc), which is $\sim$ 2 Mpc closer than our distance estimation.

Table 2 contains the object ID's of the matched PNe for both FCC167 and FCC219, with their respective m_{5007} from both our measurements, and those catalogued in Feldmeier et al. (2007) and McMillan et al. (1993) respectively. We applied a separation limit of 3.6 arcseconds for matching sources. However, within FCC 167, we had to account for a -0.4 to -0.8 arcsecond shift in Declination coordinates, which may arise from a minor inaccuracy in header information.

Table 2. List of matched source IDs from the central pointings, accompanied by both our measured m_{5007}, and those reported within the literature; FCC 167: Feldmeier et al. (2007), and FCC 219: McMillan et al. (1993).

Galaxy	ID	$m_{5007\,F3D}$	$m_{5007\,lit}$
FCC167	F3D J033627.54-345759.28	27.18	26.59
	F3D J033628.01-345814.80	26.92	26.73
	F3D J033626.37-345829.46	27.23	26.81
	F3D J033625.64-345818.91	27.61	27.20
FCC219	F3D J033849.09-353523.23	27.67	26.79
	F3D J033848.97-353520.76	27.08	26.83
	F3D J033850.08-353515.62	27.39	26.98
	F3D J033853.81-353502.60	28.23	27.54
	F3D J033849.53-353502.86	27.39	27.68

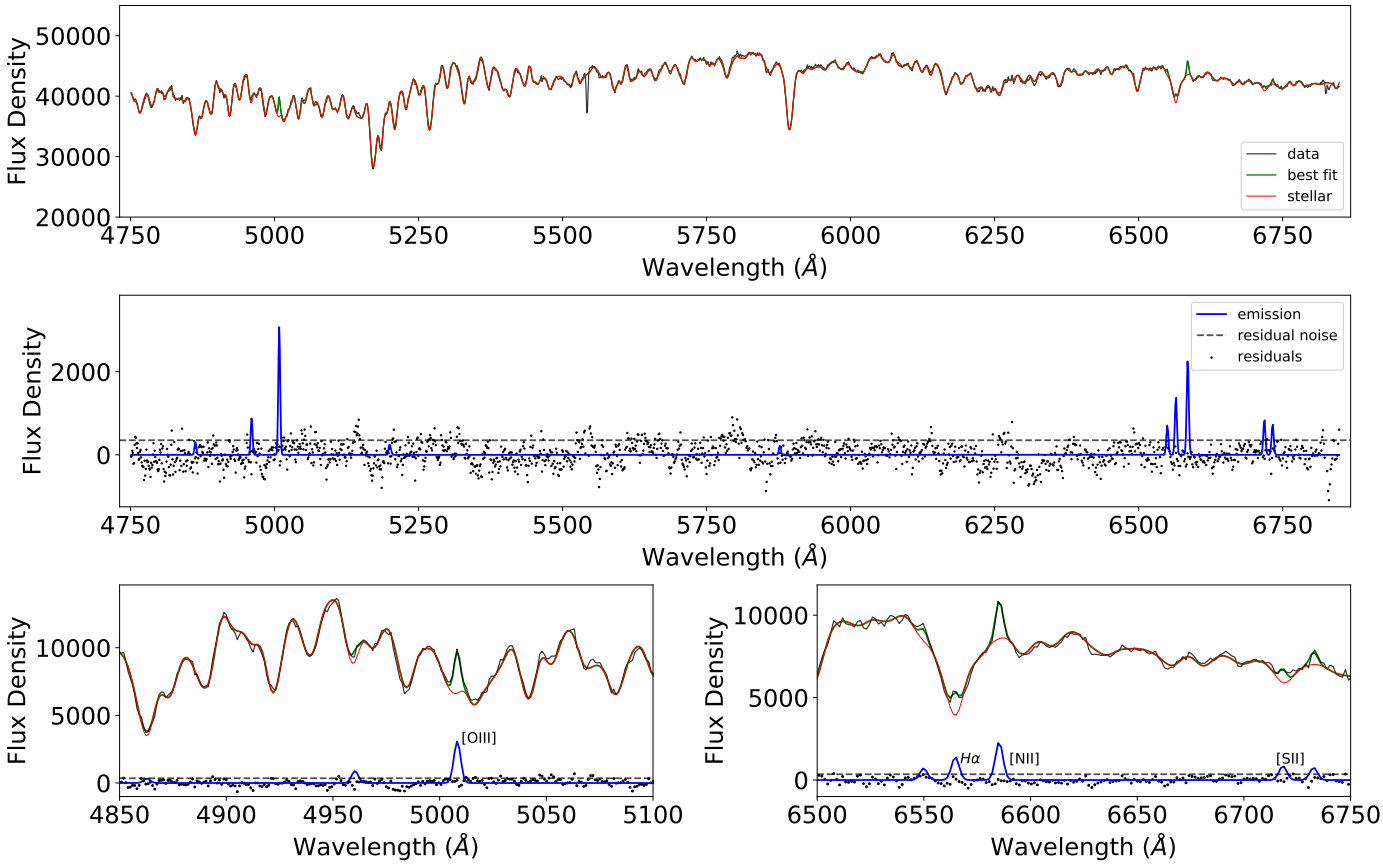

Fig. 9. Same as Fig 8 but now for potential supernova remnant source within FCC 167 (F3D J033627.66-345844.20), with detected Hα, [N II] and [S II] emission of comparable strength to [O III].

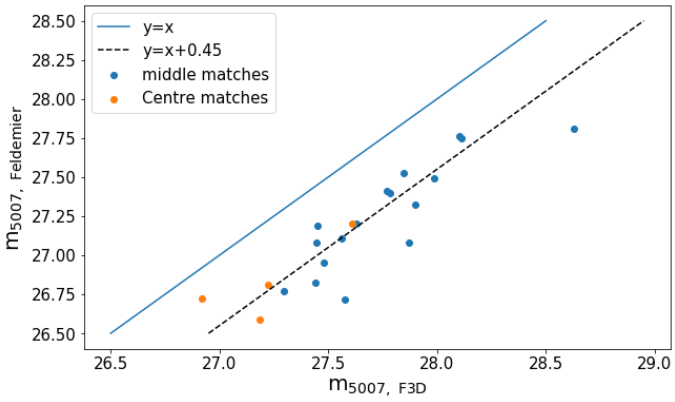

Fig. 10. Comparing the m_{5007} of PNe detected within FCC 167 (x-axis), against those matched from the Feldmeier et al. (2007) sample (y-axis). We match 21 sources, found in the central (orange) and middle (blue) pointings of the F3D FCC 167 observations. We find the comparisons to be consistent, however there is a systematic offset (dashed black line) in values, where our measured m_{5007} values are ~ 0.45 mag fainter than those of Feldmeier et al. (2007).

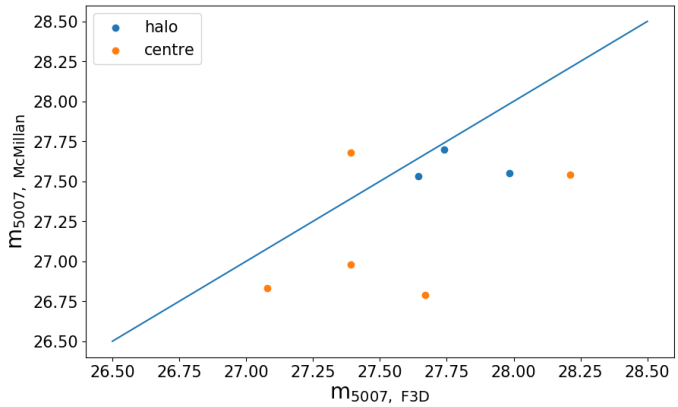

Fig. 11. The comparison of the PNe detected in FCC 219, presented here, that match with those reported by McMillan et al. (1993). Due to the low number of matches compared to that of FCC 167, we are cautious of concluding on any systematic biases, or agreements.

4. Spectral catalogue

Having arrived at a robust set of PNe candidate sources, we proceed to further characterise their spectral properties. Some of these unresolved [O III] sources may still originate from objects other than PNe. Typical PNe spectra are dominated by strong [O III] lines and little emission from other atomic species. The presence of strong Hα emission, on the other hand, could signal the presence of unresolved HII regions, whereas the additional presence of significant [N II] or [S II] emission could be indicative of a supernova remnant (SNR). A more comprehensive emission-line fit could also inform on the amount of extinction (through the Balmer decrement) and therefore lead to the dereddened absolute M_{5007} magnitude values for our target PNe, which can fall below the PNLF cut-off value ($M^*_{5007} = -4.53$ Ciardullo 2012).

In this respect, to make full use of the MUSE spectral range, for each of our confirmed candidate PNe sources we extracted

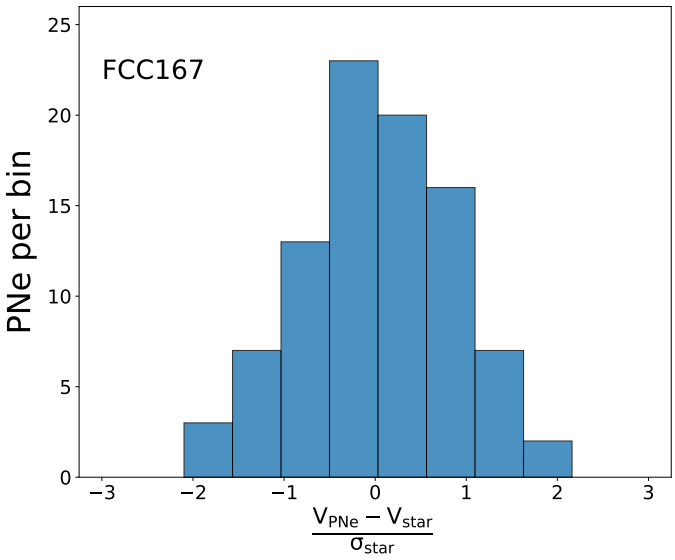

Fig. 12. Values and distribution for the $\Delta V/\sigma$ ratio for PNe within FCC 167, where dV is the difference between the PNe velocities and that of the stars in the galaxy at the PNe location and σ is the stellar velocity dispersion, also at the PNe position.

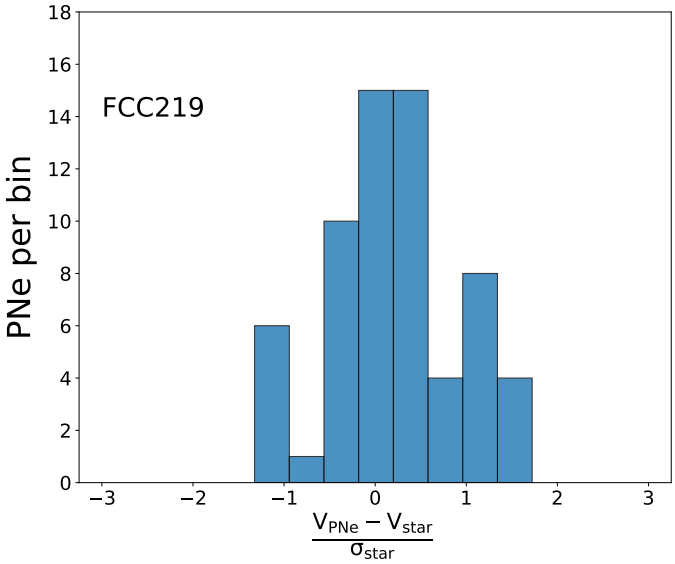

Fig. 13. FCC 219's distribution of the $\Delta V/\sigma$. Similar to Fig. 12.

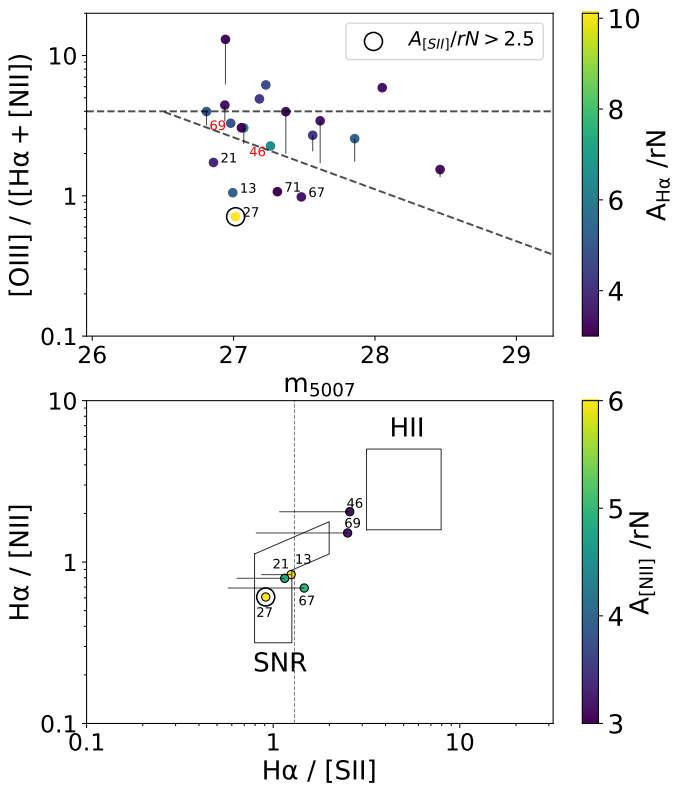

Fig. 14. Contamination diagrams for FCC 167. *Top panel:* Values for the [O III]/(Hα+[N II]) line ratio for the PNe candidate sources, as returned from our spectral fit and only for objects that were already validated for fit quality and detectability. The symbols are colour coded according to the signal to noise level of the Hα, which is the predominant line of the Hα [N II] pairing. The sources included here either passed the $A_{H\alpha}/rN$>3, or $A_{[N\,II]}/rN$>3 filter. When this is not the case, a vertical line points to the corresponding lower limit for [O III]/(Hα+[N II]), assuming an upper limit in the [N II] flux corresponding to a $A_{[N\,II]+H\alpha}/rN = 3$. Assuming a distance modulus of 31.24 mag (Sect. 5), the dashed lines show the region typically occupied by PNe according to Ciardullo et al. (2002) and Herrmann et al. (2008). *Lower panel:* position of the PNe sources with firmly detected [N II] and Hα emission in the Sabbadin et al. (1977) diagnostic diagram locating the regions occupied by PNe (from Riesgo & López (2006), SN remnants and unresolved H II-regions. Similar to the top panel, horizontal lines indicate the range of values down to a lower limits for the Hα/[S II] ratio where the [S II] doublet is not formally detected. Sources detected with S II/rN >3 are highlighted by a circle, with one such source found within FCC 167. Sources are numbered to show where they lie in relation to each other, between the two diagnostic diagrams.

a PSF-weighted MUSE aperture spectrum from the original MUSE cube at the location of our sources. We then fit each of these aperture spectra using GandALF, keeping to the local stellar kinematics as derived in Sect. 3.1 and imposing the same profile to all emission lines. In particular, here we fix the width of all lines according to the value of the intrinsic σ derived in Sect. 3.5.

Figure 8 and 9 show two examples of such GandALF fits, one for the typical spectrum of a PNe source and the other showing an example of a potential SNR impostor (Sect. 4.2). From these fits we obtained the fitted flux of Hβ, [O III] 5007, [N II] 6583, Hα and of the [S II] 6716,6731 doublet, together with their corresponding A/rN values. We report a good agreement between the [O III] flux values via our 1D+2D fitting method,from fits to these apertures, with the values differing less than 10 percent.

4.1. PNe candidate interlopers

We attempted to identify interlopers by checking whether each PN candidate's velocity, measured by the [O III] lines, is consistent with having been drawn from the local stellar line-of-sight velocity distribution (LOSVD). In Fig. 12, we plot the distribution for the ratio between the difference in the PNe candidate and local stellar velocity ($\Delta V = V_{PNe} - V_{stars}$) and the local stellar velocity dispersion (σ_{stars}). To a first approximation, without accounting for higher-order moments of the LOSVD, we indeed expect such a $\Delta V/\sigma_{stars}$ ratio to follow a Gaussian distribution for PNe candidates belonging to the galaxy. Any object with $|\Delta V/\sigma_{stars}| > 3$ should be very likely an interloper. One PNe is identified as interloping within FCC 167, and labelled as such in 4. As for FCC 219, we find no interloping PNe. For FCC 219,

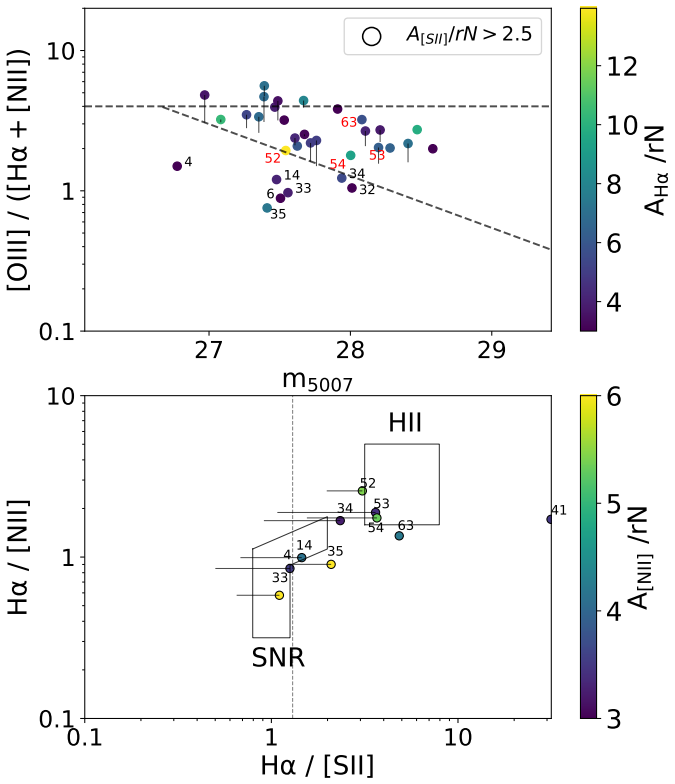

Fig. 15. Contamination diagrams for FCC 219. Using the same procedure and diagnostics as seen n Fig. 14. In the top panel, we see fewer sources residing outside the dashed lines (from Eq. 7). We do not observe any sources exhibiting [S II] emission above a signal to noise of 3. Points are again numbered to help identify sources between the two plots.

we plot the distribution of $|\Delta V/\sigma_{stars}|$(see, Fig. 13). We identify no interloping PNe within FCC219's catalogue. The distribution of PNe and their respective velocities lies within the measured velocity distribution range reported in Iodice et al. (2019a) for both galaxies.

4.2. PNe impostors

It would be reasonable to assume that for an early type galaxy, the majority of unresolved point sources detected via their [O III] emission would be PNe. However, when considering the spatial scales covered by one PSF FWHM (~ 80pc), we need to double check that the population of PN that we discover is checked for obvious contamination sources; primarily unresolved H II regions, and SNRs. Previous studies of PNe, via "on-off" band photometry, use band filters (~ 30 - 60 Å wide) designed to isolate the emission of [O III] lines. This would allow for potential of contamination sources other than those just mentioned, including both high redshift (z~3.1) Lyα emitting galaxies, background galaxies emitting [O II] 3727Å (z~0.34).

However, with IFU data, we can resolve both components of the [O III] emission (4959Å and 5007Å). This advantage is helpful in detecting and filtering the PNe from impostors; sources with only one emission line, that are fitted with a dual peak model, produce a χ^2 greater than if the source were a PNe with both emission lines. We therefore rely on the filtering methods discussed here, to exclude such objects as Lyα galaxies, or [O II] background galaxies before the contamination checks. This process has been assessed on sources that have been identified as single emission peak, and found to filter such objects out, within the fitting and filtering steps.

To address the two other sources of survey contamination, other diagnostic emission lines, namely Hβ, Hα, [N II] and [S II] must be considered and compared to the emission of [O III]. We follow the method of Kreckel et al. (2017), using the ratio of [O III] to Hα as a primary identifier between PNe sources and compact, unresolved H II regions (Eq. 7, see also Ciardullo et al. 2002; Herrmann et al. 2008; Davis et al. 2018). This comparison stems from the fact that for PN sources, the intensity of [O III] will be greater than Hα.

In the case of supernova remnant identification, we rely on the initial works of Riesgo & López (2006), and more recently Kreckel et al. (2017). One key difference in the emission line analysis of SNR compared to H II regions, is the presence of larger [S II] to Hα ratio in SNR, compared to that found in compact H II regions. SNR have been shown to exhibit similar ratios of [O III] to Hα as PNe (Davis et al. 2018), and hence require their own classifier for identification purposes. Following previous survey methods, we apply a threshold for the ratio of [S II] to Hα, where a source has to exhibit [S II] / Hα > 0.3 to be considered a SNR (Blair & Long 2004). The limiting factor in this approach is that we have to first detect [S II] emission with a signal-to-noise of three. This detection however, is not always possible. In such cases, we evaluate an upper value of the emission line ratio if the lines were above a signal-to-noise level of three.

We present the results of our contamination analysis, as seen in Fig. 14 and Fig. 15. Excluded objects are catalogued and given an appropriate ID type, in Tables 4 and 5. The top panel of Fig. 14 shows the flux ratio of [O III] and Hα+[N II], plotted against m_{5007}, along with the limits set out in Eq. 7 (Ciardullo et al. 2002):

$$4 < \log_{10}\left(\frac{F([\mathrm{O\,III}])}{F(H\alpha + [\mathrm{N\,II}])}\right) < -0.37 M_{5007} - 1.16. \quad (7)$$

Here, we find a number of sources below the "cone" region, highlighting sources with a higher than expected abundance of Hα+[N II] in comparison to [O III] for a given m_{5007}. The data points are colour coordinated with respect to the PN's $A_{H\alpha}$/rN level. Sources with detected [S II] emission with a signal to noise level higher than 2.5 of the residual noise, are highlighted by a circle. Only one [O III] emitting source, detected within FCC 167, is found to be emitting [S II] above this threshold. The lower panel of Fig. 14 presents the second impostor check that was performed. This panel has a few juxtaposed regions that help identify where certain sources would appear based on the ratios of various emission lines. For FCC 167, we identified five objects in need of exclusion: four highly-likely potential SNR and one object believed to be a compact H II region. We run the same impostor checks on FCC 219, with the results displayed in Fig. 15, noting though, no sources that present [S II] signal above 2.5 times the background. We find seven objects in total for exclusion: three highly likely SNR, and four likely H II regions objects. We also note that within the lower panel of Fig. 15 there are objects within the H II area that are not below the defining limit of the upper panel. These are believed to be PN, as there is potential for PNe to overlap such a region, where a number of PNe have been observed with greater Hα emissions, compared to the main population of PNe.

We are confident that we have reliably excluded impostor sources, without confusing background diffuse emission with that originating from the unresolved point source. This is aided

by imposing the same line profile width, as fitted from [O III], to the other fitted emission lines. This certifies that we will not report line strengths from background, diffuse ionised gas. The line profiles of such background emissions would appear wider than those originating from unresolved point sources moving with the stars. Fig. 9 displays our GandALF fit for the brightest of our SNR sources. There, we highlight a few regions of particular interest, namely around the [O III] 4956 5007ÅÅ (bottom left), Hα 6563Å, [N II] 6548 6583ÅÅ [S II] 6716 6731ÅÅ (bottom right) nebular emission lines.

5. Results and discussion

5.1. Planetary nebulae results

Within the central region of FCC 167, we catalogue 91 [O III] emitting sources, labelled as PNe. Table 4 summarises the outcome from our aforementioned filtering procedure. It presents our catalogue of the PNe sources, further plot in Fig. 1, highlighted with black circles, with the over-luminous source highlighted by a black square icon. The PNe we found to match those reported in Feldmeier et al. (2007) are highlighted by a blue square. All PNe were labelled on the basis of their identifying number. In addition, the table contains their RA and DEC (J2000), apparent magnitude in [O III] (m_{5007}), and A/rN.

Of the detected [O III] emitting sources within FCC 167's FOV, one source appears over-luminous by 0.4 mag with respect to the predicted cut-off of the PNLF. This is not so surprising and such sources have been previously reported (Jacoby et al. 1996; Longobardi et al. 2013). A few scenarios have been put forward to account for over-luminous sources. One possibility would be the "chance superposition of a number of PNe". Another statistically more favoured possibility is that such objects are the product of "coalesced binaries". Our emission line filtering did not allow for the safe identification of that particular source, albeit it hinted that such sources are less likely to be due to an H II region or a SNR. This observation is further supplemented by the fact that FCC 167 is a typical early-type galaxy with an older stellar population, expected to be dominated by low-mass stars ($\sim 1 M_{\odot}$). Within such a population we do not expect to have either very luminous H II regions or frequent SN explosions. Moreover, our spatial resolution spans ~80 pc and as such blending of PNe sources is quite likely.

As for the central observation of FCC 219, we catalogue 56 [O III] emitting sources, classifying them as PNe. of the originally detect point sources, five were deemed to be PNe impostors, though no interlopers are present. We note that the tree sources classified as SNR are closely grouped together, which may infer that the underlying stellar environment was part of a more recent star formation burst, and that the supernova may be type II. Figure 2 shows the FOV with the catalogued sources highlighted with black circles, and those that matched with McMillan et al. (1993) are again highlighted by a blue square. See Table 5 for the catalogued source's properties.

5.2. Planetary nebular luminosity function

The empirical form of the PNLF (as introduced by Ciardullo et al. 1989, Eq. 8), is described by an exponential drop off at the bright end, with an accompanying exponential tail for the fainter end. It can be approximated with the following functional form:

$$N(M) \propto e^{c_1 M_{5007}} \left[1 - e^{3(M^*_{5007} - M_{5007})}\right], \quad (8)$$

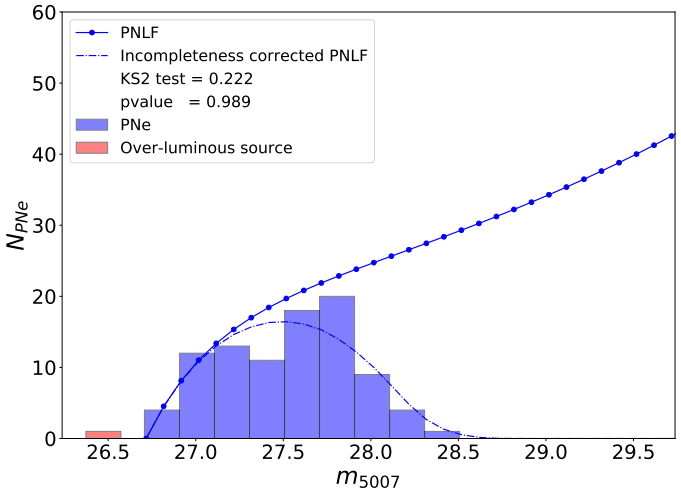

Fig. 16. The PNLF for FCC 167, is given by the binned values of m_{5007} from the PNe population.The blue solid line indicates the empirical form of the PNLF, given by Eq. 8, with the completeness corrected PNLF depicted by the dashed line. Both curves have been normalised in such a way that the integral of the incompleteness corrected PNLF matches the total number of observed PNe.

where M_{5007} is the absolute magnitude of the detected PN. M^*_{5007} is the cut-off absolute magnitude of the brightest PNe, originally calibrated to −4.48, from observations of the M31 PNe population, assuming a Cepheid distance of 710kpc (Ciardullo et al. 1989). The c_1 parameter details how the tail of the function behaves, and was derived from the model of an expanding, ionised [O III] spherical shell ($c_1 = 0.307$; Henize & Westerlund 1963). More recently, Ciardullo (2012) explored the PNLF zero-point (M^*_{5007}), calibrating its value with galaxies that already had distance estimates from Cepheid and or Tip of the Red Giant Branch (TRGB) methods. He finds an agreement between these two distance estimators with $M^*_{5007} = -4.53$, while also finding no evidence for a metallicity dependence on M^*_{5007}. Gesicki et al. (2018) further explored how star formation history, and stellar population age, could affect the bright cut-off of a detected PNe population's PNLF. Together with the recent work of Valenzuela et al. (2019), these studies finally overcome the initial difficulties of obtaining M^*_{5007} PNe in old stellar populations with mostly Solar-mass star progenitors (e.g. Marigo et al. 2004).

Another area of particular interest concerns the faint-end of the PNLF. At present, observations of Local Group galaxies, including both the Large and Small Magellanic Clouds, have yielded the exploration of the faint end of the PNLF, as such surveys would cover a greater magnitude range than galaxies beyond ~10 Mpc. Surveys such as ours are limited to the bright-end of the distribution, exploring $\sim 1-2$ mag down from the cut-off. It has been demonstrated within M31, by exploring $\sim 5-6$ mags from the cut-off, that the fainter end does increase in number (Bhattacharya et al. 2019b). They comment that this could be attributed to an older stellar population; while the bright end is dominated by a younger stellar population, formed 2-4 Gyrs ago. As such, for our investigation it is imperative to understand and account for incompleteness, reinforcing our conclusions about the observed PNLF.

To construct our PNLF, we resample our PNe in 0.2 mag bins and estimate a distance modulus by assuming that the brightest source of our sample is located at the bright cut-off, $M^*_{5007} = -4.53$, (taking the second brightest object in FCC167, see below). With this distance modulus we shift the Ciardullo

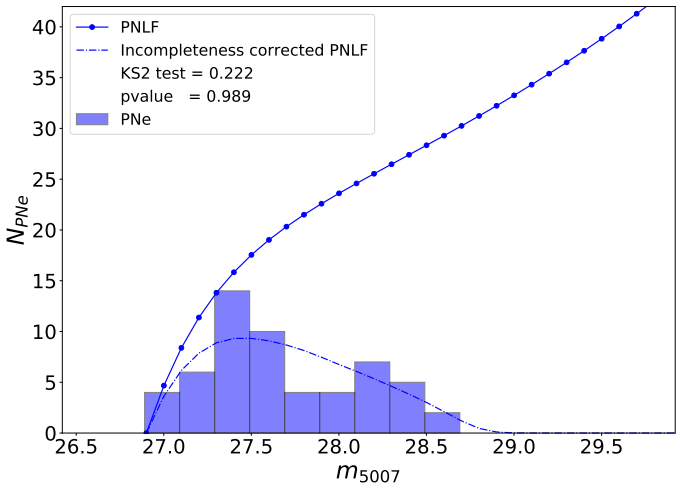

Fig. 17. The PNLF for FCC 219, shown by the binned values of m_{5007} from the catalogued PNe. Similar to Fig. 2, we plot the empirical PNLF and the completeness corrected function. We note that the observed PNLF extends further into the faint end than seen in FCC 167.

et al. (1989) predicted form of the PNLF so that it can be directly compared to our observed PNLF. This clearly suffers from the impact of incompleteness since naturally, fainter objects are expected to be lost to the noise of our spectra, either due the sky background or in the stellar continuum. Furthermore, closer to the centre of the galaxy even the brightest PNe may become undetectable, with the presence of ionised-gas occasionally complicating things further.

Within the region under consideration for constructing our PNLF (thus excluding masked regions), we define the detection completeness at any given m_{5007} magnitude as the fraction of stellar light contained in the area where PNe of that magnitude can be detected, similar to Sarzi et al. (2011) and Pastorello et al. (2013). According to our PNe detection criteria, this area includes those MUSE spaxels where the PNe peak spectral $A_{[\mathrm{O\,III}]}$ amplitude for a PNe of m_{5007} magnitude would exceed three times the local spectral residual noise level (rN) from our residual datacubes.

After computing the completeness level as a function of m_{5007} we used this function to produce an incompleteness corrected Ciardullo et al. (1989) form of the PNLF. This was then re-scaled so that its integral matched the total number of PNe in the observed PNLF.

This correction process draws on the assumption that the observed PNe are indeed drawn from the Ciardullo et al. (1989) form of the PNLF. That such incompleteness-corrected model PNLF matches well the observed PNLF of FCC167 and FCC219, shown in Fig. 16 and 17 respectively, appears to already validate such an assumption. A simple Kolmogorov-Smirnov test yields p-value = 0.99 for both FCC 167 and FCC 219, respectively, indicating in both cases that we cannot reject the null hypothesis that observed PNLF is drawn from the incompleteness-corrected Ciardullo et al. (1989) form.

5.3. Distance estimation

From the invariant cut-off in PNe luminosity, observed across different galaxies and galaxy types, we can derive a distance from converting the apparent magnitude into absolute magnitudes via the distance modulus. This distance estimation compliments the wide set of other methods such as Surface Brightness fluctuation (SBF), Supernovae Type Ia, alongside TRGB and Fundamental Plane (FP). To utilise detected PNe as a distance estimator, one requires a sufficiently large sample that has to necessarily contain the brightest PNe.

For FCC 167, returning to the over-luminous object, if we assume the source is at the cut-off for our PNe population (M^*_{5007}), the resulting distance modulus estimate is 30.9 (15.2 Mpc). This is at odds with both our PNLF distance, as well as previous distance estimates of the Fornax cluster as a whole. The cluster's distance is estimated to lie between 17–22 Mpc (Ferrarese et al. 2000; Blakeslee et al. 2009; Tully et al. 2016). Another discrepancy that the inclusion of this overly-bright source introduces, would be an apparent lack of intermediately bright PNe. The over-luminous source's m_{5007} is distinctly 0.4 mag brighter than the rest of the population, with no intermediate PN detected. For those reasons, we decided to omit this source from our catalogue and further analysis.

Assuming that the brightest PN of our filtered sample resides at the bright cut-off for the PNLF, we find a distance modulus of 31.24±0.11 (D_{PNLF} = 17.68 ± 0.91 Mpc). This value is in agreement with Tully et al. (2016) and Ferrarese et al. (2000), who report values of 31.35 ± 0.24 from Supernova Type Ia (SNIa), SBF and Fundamental Plane (FP) measurements, and 31.37 ± 0.20 from SBF and Globular Cluster LF, respectively. If, on the other hand, we were to evaluate the 91 PNe candidates at a predetermined distance of 21.2 Mpc (31.63 ± 0.08) (Blakeslee et al. 2009), who determine their distance from SBF measurements in the Sloan z-band, the distribution of PNe shifts towards the more luminous end of the PNLF, reaching $M_{5007} \approx -5.0$. This would be in contradiction of the majority, if not all previous PN surveys who find $M^*_{5007} \approx -4.5$.

For the central observation of FCC 219, we estimate a distance modulus of 31.42 ± 0.1 (19.24 ± 0.84 Mpc). This agrees, within the stated limits, with the distance from Tully et al. (2016); 31.37 ± 0.22, as well the measurements reported by Ferrarese et al. (2000); 31.22 ± 0.12. We conclude that we still reside within the cluster's expected distance range, noting that previous studies have found some discrepancies between SBF and PNLF estimates (Ciardullo 2012; Kreckel et al. 2017).

5.4. Luminosity specific planetary nebulae frequency

As discussed in Sect. 5.2, and shown in Fig 16 and 17, the observed PNLF in FCC167 and FCC219 are consistent with the Ciardullo et al. (1989) empirical form of the PNLF, once this is corrected for incompleteness and re-scaled so that its integral matches to total number of PNe we observed. By applying the same normalisation also to the original function we can similarly integrate it to estimate the total number of PNe in the regions under consideration $N_{PNLF,\Delta M}$ down to some magnitude limit ΔM. Dividing this number by the stellar bolometric luminosity in the same region (L_{Bol}), we can arrive at the luminosity specific planetary frequency:

$$\alpha_{\Delta m} = N_{PNLF,\Delta m}/L_{Bol}, \quad (9)$$

which may depend on the stellar parent population properties (e.g. Buzzoni et al. 2006). In this paper, we rely on the the commonly adopted $\alpha_{2.5}$ measurement for the luminosity specific PN frequency, where the PNLF is integrated down 2.5 magnitudes from the bright end cut-off point.

To evaluate the bolometric luminosity we first proceed to obtain an integrated spectrum of the stellar regions where the presence of PNe is being investigated (e.g. within the MUSE FOV

Table 3. Galaxy, number of PNe according to PNLF, total bolometric luminosity and $\alpha_{2.5}$.

Galaxy	$N_{PNLF,2.5}$	L_{Bol} ($10^9\ L_\odot$)	$\alpha_{2.5}$ ($10^{-8}\ N_{PNe}\ L_\odot^{-1}$)
FCC 167	277 ± 29	$16.99^{+1.82}_{-1.51}$	$1.63^{+0.24}_{-0.23}$
FCC 219	287 ± 38	$27.13^{+2.49}_{-2.21}$	$1.06^{+0.16}_{-0.17}$

excluding masked region). We then fit this spectrum with pPXF using the EMILES templates (Vazdekis et al. 2016), using the resulting template weights to reassemble an optimal template across the entire wavelength range of the EMILES templates. As this is rather extended, we can compare the total flux to that in the SDSS g-band to work out a bolometric correction for the g-band. We can then apply to g-band flux observed in our integrate spectra and thence obtain a bolometric luminosity at the distance derived from the PNLF. Table 3 presents both N_{PNLF} and L_{bol} that were used in determining $\alpha_{2.5}$.

Our estimates of $\alpha_{2.5}$ are somewhat different between the two galaxies, where the value of FCC 167 is ∼1.6 times that of FCC 219. According to Buzzoni et al. (2006), such a difference in the specific number of PNe may relate to a difference in metallicity, in the parent stellar population. However, in the case of FCC 167 and FCC 219, Iodice et al. (2019a) reports rather similar values for the central (within an effective radii, 0.5 R_e) stellar metallicity ([M/H]): 0.09 dex for FCC 167 and 0.14 dex for FCC 219. One potential source of such a difference could be the presence of hot gas halo in FCC 219 as demonstrated by X-ray data (e.g. Jones et al. 1997; Murakami et al. 2011). However, FCC 167 does not posses as significant a hot gas inter-stellar / inter-galactic medium component. The lower N_{PNLF} value reported for FCC 219 could, therefore, stem from the ram pressure the PNe gas would experience as it passes through the hot medium. This would naturally act to sweep the PNe gas associated to a central ionising star (Conroy et al. 2015). (). More effort from a modelling perspective, is still needed in elucidating the potential impact the hot X-ray halos could have on the population of PNe (e.g. following Li et al. 2019). Earlier studies of this interaction focused on the Virgo cluster, namely M87, and found evidence of re-compression of PN shells for PNe closer to the galactic nucleus (Dopita et al. 2000), whereas those PN that are ejected into the Intra-cluster medium, reported shorter evolutionary times (τ_{PN}), when compared to previous estimates (Villaver & Stanghellini 2005).

6. Conclusions

In this work, we have attempted to achieve a consensus in detecting PNe, in regards to the population of PNe in two galaxies (FCC 167 and FCC 219). For that purpose, we have developed a novel fitting and detection procedure, capable of combining both the spectra and spatial information contained in our IFU observations. In it, the spatial information is portrayed by a Moffat distribution function. We further demonstrated it is capable of also successfully accounting for the [O III] spectral emission lines. With our procedure we could either fix or infer the instrumental PSF. Moreover, we ran an extensive set of simulations to constrain its limitation, in particular, concerning our MUSE observations. We have illustrated the capabilities of this newly developed procedure by applying it to two galaxies.

The primary outcomes of the analysis carried out on FCC 167 and FCC 219 include:

- A catalogue of 91 detected [O III] unresolved point sources, characterised here as PNe in origin, within FCC 167, and 56 PNe within FCC 219.
- Through the use of the presented modelling techniques, we have accurately reproduced the PSF of each pointing, having fitted multiple PNe in parallel, with the same PSF shape. This improves the accuracy of the reported [O III] flux values.
- Through simulations of modelling known PNe, we have tested and verified the reliability of our results, as well as the accuracy of the parameters used within the presented 1D+2D modelling technique. This investigation also highlighted the limitations in A/rN that must be factored in when filtering for outliers. We are confident in our method's results for categorising sources as PNe, when measured above A/rN of 3.
- Via emission line ratio diagnostics and comparing the velocity of the PNe to the background stellar populations, we have identified one interloper, and five potential impostors within our FCC 167 sample: four SNR and one compact H II region. For FCC 219, we identify three SNR and four likely compact H II regions, with no evidence of any interloping PNe within the catalogue.
- We have calculated the values for the luminosity specific planetary nebulae frequency, $\alpha_{2.5}$, for the population of PNe down to 2.5 mags from the bright end cut-off, for both FCC 167 and FCC 219: $1.63^{+0.24}_{-0.23} \times 10^{-8}$ and $1.06^{+0.16}_{-0.17} \times 10^{-8}$ respectively.
- Finally, through the use of the PNLF and the invariant cut-off in brightness, for the PNe, we report distances to the host galaxies: 17.68 ± 0.91 Mpc for FCC 167, and 19.24 ± 0.84 Mpc for FCC 219. Both distance estimates agree with current literature, consistent with other methods that utilise Surface Brightness Fluctuations and SNIa measurements. They also agree within the limits of the distance to the Fornax cluster (17–22Mpc)

Moving forward, we are primed to explore the rest of the bright ETG population within the Fornax 3D survey. Cataloguing the positions, magnitudes and emission line ratios of their PNe populations within the central regions. Then, once the catalogue of ETG's has been evaluated, we will compare distance estimates from the PNLF with other current methods. The primary scientific analysis will consist of comparing each galaxy's $\alpha_{2.5}$ value with their relative galactic properties: UV excess, metallicity and other such properties that would impact on stellar evolution, and hence PNe formation.

Acknowledgements. We would like to thank the referee for their constructive responses, which has improved the content and clarity of this manuscript. Based on observations collected at the European Southern Observatory under ESO programme 296.B-5054(A). TS thanks A. Bittner, A. Jones and R. Jackson and M. Timberhill for their help and ideas that aided in the construction and presentation of this paper. This work was supported by Science and Technology Facilities Council [grant number ST/R504786/1]. RMcD is the recipient of an Australian Research Council Future Fellowship (project number FT150100333). J. F-B acknowledges support through the RAVET project by the grant AYA2016-77237-C3-1-P from the Spanish Ministry of Science, Innovation and Universities (MCIU) and through the IAC project TRACES which is partially supported through the state budget and the regional budget of the Consejería de Economía, Industria, Comercio y Conocimiento of the Canary Islands Autonomous Community. GvdV acknowledges funding from the European Research Council (ERC) under the European Union's Horizon 2020 research and innovation programme under grant agreement No 724857 (Consolidator Grant ArcheoDyn). This project made use of the following software packages: LMfit (Newville et al. 2014, 2019), Astropy, a community-developed core Python package for Astronomy (Robitaille et al. 2013), scipy (Eric Jones and Travis Oliphant and Pearu

Peterson and et al. 2001), Numpy (Van Der Walt et al. 2011), matplotlib (Hunter 2007) and Pandas (Mckinney 2010).

References

Bacon, R., Accardo, M., Adjali, L., et al. 2010, in Ground-based and Airborne Instrumentation for Astronomy III, ed. I. S. McLean, S. K. Ramsay, & H. Takami, Vol. 7735, 773508

Bacon, R., Copin, Y., Monnet, G., et al. 2001, Monthly Notices of the Royal Astronomical Society, 326, 23

Bertin, E. & Arnouts, S. 1996, A&A, 117, 393

Bhattacharya, S., Arnaboldi, M., Caldwell, N., et al. 2019a, Astronomy and Astrophysics, 631

Bhattacharya, S., Arnaboldi, M., Hartke, J., et al. 2019b, A&A, 624

Bittner, A., Falcón-Barroso, J., Nedelchev, B., et al. 2019, Astronomy & Astrophysics, 628, A117

Blair, W. P. & Long, K. S. 2004, The Astrophysical Journal Supplement Series, 155, 101

Blakeslee, J. P., Jordán, A., Mei, S., et al. 2009, The Astrophysical Journal, 694, 556

Bundy, K., Bershady, M. A., Law, D. R., et al. 2014, The Astrophysical Journal, 798, 7

Buzzoni, A., Arnaboldi, M., & Corradi, R. L. M. 2006, Mon. Not. R. Astron. Soc, 000, 1

Cappellari, M. 2017, Monthly Notices of the Royal Astronomical Society, 466, 798

Cappellari, M. & Copin, Y. 2003, Monthly Notices of the Royal Astronomical Society, 342, 345

Cappellari, M. & Emsellem, E. 2004, Publications of the Astronomical Society of the Pacific, 116, 138

Ciardullo, R. 2012, The Planetary Nebula Luminosity Function at the Dawn of Gaia, Tech. rep., The Pennsylvania State University

Ciardullo, R., Feldmeier, J. J., Jacoby, G. H., et al. 2002, The Astrophysical Journal, 577, 31

Ciardullo, R., Jacoby, G. H., Ford, H. C., & Neill, J. D. 1989, The Astrophysical Journal, 339, 53

Coccato, L., Gerhard, O., Arnaboldi, M., et al. 2009, Monthly Notices of the Royal Astronomical Society

Conroy, C., Van Dokkum, P. G., & Kravtsov, A. 2015, Astrophysical Journal, 803, 1

Cortesi, A., Arnaboldi, M., Coccato, L., et al. 2013, A&A

Davis, B. D., Ciardullo, R., Feldmeier, J. J., & Jacoby, G. H. 2018, Research Notes of the AAS, 2, 32

Dopita, M. A., Jacoby, G. H., Vassiliadis, E., et al. 1992, The Astrophysical Journal, 389, 27

Dopita, M. A., Massaglia, S., Bodo, G., Arnaboldi, M., & Merluzzi, P. 2000, in Astronomical Society of the Pacific Conference Series, Vol. 199, Asymmetrical Planetary Nebulae II: From Origins to Microstructures, ed. J. H. Kastner, N. Soker, & S. Rappaport (ASP Conference Series), 423

Douglas, N., Arnaboldi, M., Freeman, K., et al. 2002, Publications of the Astronomical Society of the Pacific, 114, 1234

Douglas, N. G., Napolitano, N. R., Romanowsky, A. J., et al. 2007, The Astrophysical Journal, 664, 257

Eric Jones and Travis Oliphant and Pearu Peterson and et al. 2001, SciPy: Open Source Scientific Tools for Python

Fahrion, K., Lyubenova, M., van de Ven, G., et al. 2019, Astronomy & Astrophysics, 628, A92

Feldmeier, J. J., Jacoby, G. H., & Phillips, M. M. 2007, The Astrophysical Journal, 657, 76

Ferrarese, L., Mould, J. R., Kennicutt, Jr., R. C., et al. 2000, The Astrophysical Journal, 529, 745

Freudling, W., Romaniello, M., Bramich, D. M., et al. 2013, A&A, 559, A96

Gerhard, O., Arnaboldi, M., Freeman, K. C., et al. 2005, The Astrophysical Journal, 621, L93

Gesicki, K. M., Zijlstra, A. A., & Bertolami, M. M. M. 2018, Nature Astronomy, 2, 580

Guérou, A., Krajnović, D., Epinat, B., et al. 2017, A&A, 608, A5

Hajian, A. R., Movit, S. M., Trofimov, D., et al. 2007, The Astrophysical Journal Supplement Series, 169, 289

Henize, K. G. & Westerlund, B. E. 1963, The Astrophysical Journal, 137, 747

Herrmann, K. A., Ciardullo, R., Feldmeier, J. J., & Vinciguerra, M. 2008, The Astrophysical Journal, 683, 630

Hunter, J. D. 2007, Computing in Science and Engineering, 9, 99

Iodice, E., Sarzi, M., Bittner, A., et al. 2019a, A&A, 627, A136

Iodice, E., Spavone, M., Capaccioli, M., et al. 2019b, A&A, 623, A1

Jacoby, G. H., Ciardullo, R., & Harris, W. E. 1996, The Astrophysical Journal

Jones, C., Stern, C., Forman, W., et al. 1997, The Astrophysical Journal, 482, 143

Kafle, P. R., Sharma, S., Lewis, G. F., Robotham, A. S. G., & Driver, S. P. 2018, Monthly Notices of the Royal Astronomical Society, 475, 4043

Kreckel, K., Groves, B., Bigiel, F., et al. 2017, The Astrophysical Journal, 834, 174

Li, Y., Bryan, G. L., & Quataert, E. 2019, arXiv e-prints

Longobardi, A., Arnaboldi, M., Gerhard, O., et al. 2013, a&a, 558, 42

Longobardi, A., Arnaboldi, M., Gerhard, O., Pulsoni, C., & Söldner-Rembold, I. 2018, Astronomy and Astrophysics, 620

Machacek, M., Dosaj, A., Forman, W., et al. 2005, The Astrophysical Journal, 621, 663

Marigo, P., Girardi, L., Weiss, A., Groenewegen, M. a. T., & Chiosi, C. 2004, A&A, 423, 995

Martin, T. B., Drissen, L., & Melchior, A. L. 2018, Monthly Notices of the Royal Astronomical Society, 473, 4130

Mckinney, W. 2010, Data Structures for Statistical Computing in Python, Tech. rep., AQR Capital Management

McMillan, R., Ciardullo, R., & Jacoby, G. H. 1993, The Astrophysical Journal, 416, 62

Moffat, A. F. J. 1969, A&A, 3, 455

Murakami, H., Komiyama, M., Matsushita, K., et al. 2011, Publications of the Astronomical Society of Japan, 63, S963

Newville, M., Otten, R., Nelson, A., et al. 2019, lmfit/lmfit-py 1.0.0, Tech. rep., University of Chicago

Newville, M., Stensitzki, T., Allen, D. B., & Ingargiola, A. 2014, LMFIT: Non-Linear Least-Square Minimization and Curve-Fitting for Python¶, Tech. rep., University of Chicago

Paczyński, B., Paczyński, & B. 1971, Acta Astronomica, 21, 417

Pastorello, N., Sarzi, M., Cappellari, M., et al. 2013, Monthly Notices of the Royal Astronomical Society, 430, 1219

Pulsoni, C., Gerhard, O., Arnaboldi, M., et al. 2018, Astronomy and Astrophysics, 618

Ricci, T. V., Steiner, J. E., & Menezes, R. B. 2016, Monthly Notices of the Royal Astronomical Society, 463, 3860

Riesgo, H. & López, J. A. 2006, Revised Diagnostic Diagrams for Planetary Nebulae, Tech. rep., Instituto de Astronomía Universidad Nacional Autónoma de México, Ensenada, B.C., México

Robitaille, T. P., Tollerud, E. J., Greenfield, P., et al. 2013, Astronomy and Astrophysics, 558

Romanowsky, A. J., Douglas, N. G., Arnaboldi, M., et al. 2003, Science, 301, 1696

Roth, M. M., Kelz, A., Fechner, T., et al. 2005, Publications of the Astronomical Society of the Pacific, 117, 620

Sabbadin, F., Minello, S., & Bianchini, A. 1977, A&A, 60, 147

Sanchez, S. F., Kennicutt, R. C., de Paz, A. G., et al. 2011, A&A, 538, A8

Sánchez-Blázquez, P., Peletier, R. F., Jiménez-Vicente, J., et al. 2006, Monthly Notices of the Royal Astronomical Society, 371, 703

Sarzi, M., Falcón-Barroso, J., Davies, R. L., et al. 2006, Monthly Notices of the Royal Astronomical Society, 366, 1151

Sarzi, M., Iodice, E., Coccato, L., et al. 2018, Astrophysics A&A, 616, 121

Sarzi, M., Mamon, G. A., Cappellari, M., et al. 2011, Monthly Notices of the Royal Astronomical Society, 415, 2832

Schönberner, D., Jacob, R., Lehmann, H., et al. 2014, Astronomische Nachrichten, 335, 378

Soto, K. T., Lilly, S. J., Bacon, R., Richard, J., & Conseil, S. 2016, Monthly Notices of the Royal Astronomical Society, 458, 3210

Spriggs, T. 2020, tspriggs/MUSE_PNe_fitting: MUSE focused Planetary Nebulae detection and fitting

Su, Y., Nulsen, P. E. J., Kraft, R. P., et al. 2017, The Astrophysical Journal, 851, 69

Tully, R. B., Courtois, H. M., & Sorce, J. G. 2016, The Astronomical Journal, 152, 50

Valenzuela, L. M., Méndez, R. H., & Miller Bertolami, M. M. 2019, The Astrophysical Journal, 887, 65

Van Der Walt, S., Colbert, S. C., & Varoquaux, G. 2011, Computing in Science and Engineering, 13, 22

Vazdekis, A., Koleva, M., Ricciardelli, E., Röck, B., & Falcón-Barroso, J. 2016, Monthly Notices of the Royal Astronomical Society, 463, 3409

Ventimiglia, G., Arnaboldi, M., & Gerhard, O. 2011, Astronomy and Astrophysics, 528

Viaene, S., Sarzi, M., Zabel, N., et al. 2019, A&A, 622, A89

Villaver, E. & Stanghellini, L. 2005, The Astrophysical Journal, 632, 854

Weijmans, A. M., Cappellari, M., Bacon, R., et al. 2009, Monthly Notices of the Royal Astronomical Society, 398, 561

Weilbacher, P. M., Streicher, O., & Palsa, R. 2016, Astrophysics Source Code Library, ascl:1610.004

Weilbacher, P. M., Streicher, O., Urrutia, T., et al. 2012, in Software and Cyberinfrastructure for Astronomy II, ed. N. M. Radziwill & G. Chiozzi, Vol. 8451, 84510B

Weinberger, R., Dengel, J., Hartl, H., & Sabbadin, F. 1983, The Astrophysical Journal, 265, 249

York, D. G., Adelman, J., Anderson, Jr., J. E., et al. 2000, The Astronomical Journal, 120, 1579

Table 4. Source catalogue for FCC 167: Source ID (using the IAU standard, with the Fornax3D; F3D, prefix), RA and Dec, magnitude in [O III] 5007Å, signal to residual noise, line of sight velocity (km/s^{-1}) and Object ID label (PNe, SNR, H II, OvLu (Over-Luminous) or Interl (Interloper)

Source ID	RA (J2000)	Dec (J2000)	m_{5007}	A/rN	LOSV km/s^{-1}	Identifier
F3D J033627.73-345910.05	03h36m27.73s	-34d59m10.05s	27.36	6.8	-4.7	PN
F3D J033627.89-345909.52	03h36m27.89s	-34d59m09.52s	27.98	3.9	146.4	PN
F3D J033628.18-345906.71	03h36m28.18s	-34d59m06.71s	27.59	5.4	-53.5	PN
F3D J033627.24-345905.41	03h36m27.24s	-34d59m05.41s	27.43	5.9	-21.8	PN
F3D J033627.35-345903.32	03h36m27.35s	-34d59m03.32s	28.02	3.8	44.7	PN
F3D J033628.37-345901.23	03h36m28.37s	-34d59m01.23s	27.85	4.6	-24.6	PN
F3D J033626.74-345858.22	03h36m26.74s	-34d58m58.22s	27.23	6.9	286.3	PN
F3D J033626.86-345857.13	03h36m26.86s	-34d58m57.13s	27.57	5.1	170.1	PN
F3D J033626.52-345855.41	03h36m26.52s	-34d58m55.41s	27.83	3.9	96.9	PN
F3D J033628.85-345854.38	03h36m28.85s	-34d58m54.38s	28.22	3.2	72.1	PN
F3D J033628.61-345854.47	03h36m28.61s	-34d58m54.47s	26.81	11.5	66.5	PN
F3D J033628.42-345853.26	03h36m28.42s	-34d58m53.26s	27.56	5.4	40.3	PN
F3D J033626.56-345852.52	03h36m26.56s	-34d58m52.52s	27.74	4.3	121.3	PN
F3D J033627.38-345851.95	03h36m27.38s	-34d58m51.95s	26.99	7.0	253.5	SNR
F3D J033627.96-345851.01	03h36m27.96s	-34d58m51.01s	27.04	6.7	242.9	PN
F3D J033626.72-345850.83	03h36m26.72s	-34d58m50.83s	26.96	8.1	76.1	PN
F3D J033628.91-345850.36	03h36m28.91s	-34d58m50.36s	27.07	9.7	-64.3	PN
F3D J033628.25-345849.02	03h36m28.25s	-34d58m49.02s	27.67	4.0	216.2	PN
F3D J033628.82-345848.86	03h36m28.82s	-34d58m48.86s	27.33	7.5	68.5	PN
F3D J033628.51-345848.87	03h36m28.51s	-34d58m48.87s	26.94	9.4	-233.3	PN
F3D J033628.09-345848.52	03h36m28.09s	-34d58m48.52s	27.78	3.4	-106.8	PN
F3D J033627.62-345848.02	03h36m27.62s	-34d58m48.02s	26.86	7.0	87.8	SNR
F3D J033627.80-345847.73	03h36m27.80s	-34d58m47.73s	26.37	11.8	15.3	OvLu
F3D J033629.51-345847.30	03h36m29.51s	-34d58m47.30s	27.35	8.3	-158.6	PN
F3D J033625.83-345846.44	03h36m25.83s	-34d58m46.44s	27.94	4.1	126.7	PN
F3D J033626.22-345845.85	03h36m26.22s	-34d58m45.85s	27.97	3.7	235.1	PN
F3D J033629.86-345844.61	03h36m29.86s	-34d58m44.61s	27.07	10.9	54.8	PN
F3D J033627.66-345844.20	03h36m27.66s	-34d58m44.20s	27.01	5.4	72.7	SNR
F3D J033627.03-345843.97	03h36m27.03s	-34d58m43.97s	27.3	4.8	180.5	PN
F3D J033628.55-345843.71	03h36m28.55s	-34d58m43.71s	27.48	5.3	165.1	PN
F3D J033629.44-345842.94	03h36m29.44s	-34d58m42.94s	27.78	5.6	214.8	PN
F3D J033626.33-345842.12	03h36m26.33s	-34d58m42.12s	27.74	4.3	122.2	PN
F3D J033627.94-345841.88	03h36m27.94s	-34d58m41.88s	27.11	5.1	119.3	PN
F3D J033626.52-345841.28	03h36m26.52s	-34d58m41.28s	27.61	4.2	-94.8	PN
F3D J033630.12-345839.95	03h36m30.12s	-34d58m39.95s	27.77	6.2	91.3	PN
F3D J033629.09-345839.34	03h36m29.09s	-34d58m39.34s	27.87	4.4	200.7	PN
F3D J033628.76-345838.86	03h36m28.76s	-34d58m38.86s	27.73	4.1	147.8	PN
F3D J033626.28-345838.71	03h36m26.28s	-34d58m38.71s	26.94	8.5	-77.5	PN
F3D J033629.49-345838.25	03h36m29.49s	-34d58m38.25s	28.05	4.3	226.0	PN
F3D J033630.67-345837.91	03h36m30.67s	-34d58m37.91s	27.64	5.4	199.7	Interl
F3D J033628.99-345837.30	03h36m28.99s	-34d58m37.30s	27.12	8.4	21.4	PN
F3D J033626.77-345836.20	03h36m26.77s	-34d58m36.20s	27.13	5.5	45.7	PN
F3D J033626.25-345834.92	03h36m26.25s	-34d58m34.92s	27.86	3.8	-63.4	PN
F3D J033627.94-345834.66	03h36m27.94s	-34d58m34.66s	26.79	5.0	-47.2	PN
F3D J033625.92-345834.95	03h36m25.92s	-34d58m34.95s	27.76	5.0	-23.4	PN
F3D J033625.30-345834.84	03h36m25.30s	-34d58m34.84s	28.04	4.9	99.5	PN
F3D J033628.56-345834.64	03h36m28.56s	-34d58m34.64s	27.26	5.6	-83.1	PN
F3D J033626.76-345834.29	03h36m26.76s	-34d58m34.29s	27.04	5.7	208.9	PN
F3D J033626.35-345833.63	03h36m26.35s	-34d58m33.63s	27.5	5.1	-2.0	PN
F3D J033627.08-345832.69	03h36m27.08s	-34d58m32.69s	26.71	5.8	-66.3	PN

Table 4. FCC 167 - Table 1 continues

Source ID	RA (J2000)	Dec (J2000)	m_{5007}	A/rN	LOSV km/s^{-1}	Identifier
F3D J033628.10-345832.23	03h36m28.10s	-34d58m32.23s	27.06	5.0	95.6	PN
F3D J033626.95-345832.23	03h36m26.95s	-34d58m32.23s	26.85	5.7	118.4	PN
F3D J033624.62-345832.02	03h36m24.62s	-34d58m32.02s	28.12	4.2	-205.6	PN
F3D J033628.87-345831.37	03h36m28.87s	-34d58m31.37s	27.57	5.1	-108.4	PN
F3D J033630.54-345831.01	03h36m30.54s	-34d58m31.01s	28.18	4.3	-54.0	PN
F3D J033628.41-345829.74	03h36m28.41s	-34d58m29.74s	27.23	5.3	-141.4	PN
F3D J033630.27-345829.73	03h36m30.27s	-34d58m29.73s	28.46	3.6	29.6	PN
F3D J033626.37-345829.46	03h36m26.37s	-34d58m29.46s	27.23	6.5	93.8	PN
F3D J033626.44-345827.49	03h36m26.44s	-34d58m27.49s	27.24	6.6	-103.3	PN
F3D J033627.25-345827.11	03h36m27.25s	-34d58m27.11s	26.92	4.9	-102.9	PN
F3D J033628.71-345825.12	03h36m28.71s	-34d58m25.12s	27.76	4.0	-126.8	PN
F3D J033628.40-345824.77	03h36m28.40s	-34d58m24.77s	27.15	6.1	-44.1	PN
F3D J033625.66-345823.95	03h36m25.66s	-34d58m23.95s	28.04	4.4	-69.2	PN
F3D J033627.08-345823.30	03h36m27.08s	-34d58m23.30s	27.42	4.4	247.1	PN
F3D J033626.87-345822.51	03h36m26.87s	-34d58m22.51s	27.89	3.1	123.1	PN
F3D J033628.61-345822.02	03h36m28.61s	-34d58m22.02s	27.56	4.6	-125.3	PN
F3D J033626.05-345821.75	03h36m26.05s	-34d58m21.75s	27.81	4.8	91.8	PN
F3D J033628.31-345821.65	03h36m28.31s	-34d58m21.65s	27.48	4.5	-18.0	SNR
F3D J033629.10-345820.32	03h36m29.10s	-34d58m20.32s	27.86	4.7	-107.5	PN
F3D J033628.32-345820.32	03h36m28.32s	-34d58m20.32s	26.98	7.6	-38.9	PN
F3D J033626.15-345819.79	03h36m26.15s	-34d58m19.79s	27.53	6.3	-160.2	PN
F3D J033627.49-345819.56	03h36m27.49s	-34d58m19.56s	27.31	4.7	-84.3	HII
F3D J033626.87-345819.12	03h36m26.87s	-34d58m19.12s	27.49	5.0	59.3	PN
F3D J033628.75-345818.61	03h36m28.75s	-34d58m18.61s	27.59	5.0	-40.4	PN
F3D J033625.64-345818.91	03h36m25.64s	-34d58m18.91s	27.61	6.1	-18.7	PN
F3D J033627.28-345818.44	03h36m27.28s	-34d58m18.44s	27.46	4.2	-164.7	PN
F3D J033626.91-345817.42	03h36m26.91s	-34d58m17.42s	27.67	4.3	133.6	PN
F3D J033626.76-345816.31	03h36m26.76s	-34d58m16.31s	27.29	6.5	-294.4	PN
F3D J033628.35-345816.18	03h36m28.35s	-34d58m16.18s	27.5	4.9	-151.2	PN
F3D J033627.71-345815.01	03h36m27.71s	-34d58m15.01s	27.73	3.8	-85.6	PN
F3D J033629.20-345814.64	03h36m29.20s	-34d58m14.64s	27.56	6.2	-156.1	PN
F3D J033628.01-345814.80	03h36m28.01s	-34d58m14.80s	26.92	7.9	-29.1	PN
F3D J033626.38-345813.66	03h36m26.38s	-34d58m13.66s	27.82	4.9	-110.7	PN
F3D J033628.73-345812.03	03h36m28.73s	-34d58m12.03s	27.61	5.3	-128.3	PN
F3D J033626.06-345810.24	03h36m26.06s	-34d58m10.24s	27.64	5.3	72.1	PN
F3D J033628.16-345809.94	03h36m28.16s	-34d58m09.94s	27.56	5.0	-23.9	PN
F3D J033626.90-345809.61	03h36m26.90s	-34d58m09.61s	27.3	7.0	-176.6	PN
F3D J033627.61-345807.94	03h36m27.61s	-34d58m07.94s	27.76	4.1	-121.4	PN
F3D J033626.54-345806.88	03h36m26.54s	-34d58m06.88s	27.98	4.0	-135.0	PN
F3D J033628.83-345806.07	03h36m28.83s	-34d58m06.07s	28.14	3.5	-144.0	PN
F3D J033627.26-345805.81	03h36m27.26s	-34d58m05.81s	27.87	4.1	-198.8	PN
F3D J033627.52-345805.34	03h36m27.52s	-34d58m05.34s	27.37	6.2	-60.0	PN
F3D J033627.81-345803.25	03h36m27.81s	-34d58m03.25s	28.09	3.5	-125.1	PN
F3D J033627.66-345800.30	03h36m27.66s	-34d58m00.30s	27.9	4.3	-73.3	PN
F3D J033627.54-345759.28	03h36m27.54s	-34d57m59.28s	27.18	8.8	-180.0	PN
F3D J033628.26-345757.25	03h36m28.26s	-34d57m57.25s	27.69	3.8	-67.9	PN
F3D J033627.19-345756.35	03h36m27.19s	-34d57m56.35s	27.61	4.9	-229.5	PN
F3D J033627.55-345754.89	03h36m27.55s	-34d57m54.89s	26.94	11.4	-255.8	PN

Table 5. Source catalogue for FCC 219: Source ID (using the IAU standard, with the Fornax3D; F3D, prefix), RA and Dec, magnitude in [O III] 5007Å, signal to residual noise, line of sight velocity (km/s^{-1}) and Object ID label (PNe, SNR, H II or OvLu (over-luminous))

Source ID	RA (J2000)	Dec (J2000)	m_{5007}	A/rN	LOSV km/s^{-1}	Identifier
F3D J033850.92-353547.60	03h38m50.92s	-35d35m47.60s	27.53	4.5	267.7	PN
F3D J033852.44-353546.85	03h38m52.44s	-35d35m46.85s	27.22	4.2	-15.5	PN
F3D J033852.36-353544.11	03h38m52.36s	-35d35m44.11s	26.96	4.6	-36.6	PN
F3D J033850.47-353543.65	03h38m50.47s	-35d35m43.65s	26.97	9.6	-28.6	PN
F3D J033852.63-353543.31	03h38m52.63s	-35d35m43.31s	26.77	6.3	72.5	HII
F3D J033851.40-353543.11	03h38m51.40s	-35d35m43.11s	27.09	4.4	89.0	PN
F3D J033852.78-353541.32	03h38m52.78s	-35d35m41.32s	27.51	3.8	52.5	HII
F3D J033851.16-353540.22	03h38m51.16s	-35d35m40.22s	27.45	3.6	72.3	PN
F3D J033850.33-353540.40	03h38m50.33s	-35d35m40.40s	27.4	6.4	-87.0	PN
F3D J033852.87-353539.68	03h38m52.87s	-35d35m39.68s	27.37	4.7	68.8	PN
F3D J033850.70-353539.85	03h38m50.70s	-35d35m39.85s	27.38	5.6	-295.7	PN
F3D J033852.82-353537.07	03h38m52.82s	-35d35m37.07s	27.46	4.3	296.4	PN
F3D J033850.80-353536.51	03h38m50.80s	-35d35m36.51s	27.39	5.4	-138.8	PN
F3D J033849.77-353534.89	03h38m49.77s	-35d35m34.89s	28.24	3.7	-16.2	PN
F3D J033853.12-353534.39	03h38m53.12s	-35d35m34.39s	27.48	5.4	22.7	SNR
F3D J033850.44-353534.29	03h38m50.44s	-35d35m34.29s	27.47	6.0	109.5	PN
F3D J033852.17-353532.42	03h38m52.17s	-35d35m32.42s	27.18	3.9	-77.2	PN
F3D J033848.82-353531.51	03h38m48.82s	-35d35m31.51s	27.65	7.9	4.2	PN
F3D J033853.52-353531.15	03h38m53.52s	-35d35m31.15s	27.53	6.1	-49.5	PN
F3D J033851.81-353530.30	03h38m51.81s	-35d35m30.30s	26.89	5.5	-13.9	PN
F3D J033852.48-353529.87	03h38m52.48s	-35d35m29.87s	27.29	5.2	-48.2	PN
F3D J033853.79-353529.58	03h38m53.79s	-35d35m29.58s	27.27	5.8	-226.8	PN
F3D J033850.32-353527.88	03h38m50.32s	-35d35m27.88s	27.16	8.8	197.6	PN
F3D J033852.01-353527.29	03h38m52.01s	-35d35m27.29s	27.37	4.3	75.1	PN
F3D J033851.76-353526.69	03h38m51.76s	-35d35m26.69s	27.45	4.3	-169.3	PN
F3D J033852.62-353526.91	03h38m52.62s	-35d35m26.91s	27.36	5.7	-90.7	PN
F3D J033853.71-353525.47	03h38m53.71s	-35d35m25.47s	28.33	3.3	221.7	PN
F3D J033850.03-353525.45	03h38m50.03s	-35d35m25.45s	27.68	6.3	-45.9	PN
F3D J033851.74-353525.08	03h38m51.74s	-35d35m25.08s	27.68	3.8	83.4	PN
F3D J033853.20-353523.94	03h38m53.20s	-35d35m23.94s	27.76	5.0	202.1	PN
F3D J033851.56-353523.60	03h38m51.56s	-35d35m23.60s	27.7	4.2	121.3	PN
F3D J033849.09-353523.23	03h38m49.09s	-35d35m23.23s	27.67	8.0	-254.3	PN
F3D J033852.17-353522.75	03h38m52.17s	-35d35m22.75s	28.01	3.5	13.4	HII
F3D J033852.35-353522.53	03h38m52.35s	-35d35m22.53s	27.56	5.1	-32.0	SNR
F3D J033850.76-353520.79	03h38m50.76s	-35d35m20.79s	27.94	4.7	-155.1	HII
F3D J033852.21-353520.77	03h38m52.21s	-35d35m20.77s	27.41	6.2	-108.1	SNR
F3D J033848.97-353520.76	03h38m48.97s	-35d35m20.76s	27.08	14.7	109.6	PN
F3D J033853.85-353519.20	03h38m53.85s	-35d35m19.20s	27.82	5.9	24.4	PN
F3D J033851.97-353518.34	03h38m51.97s	-35d35m18.34s	27.61	5.7	34.1	PN
F3D J033851.82-353517.93	03h38m51.82s	-35d35m17.93s	27.72	5.3	-45.5	PN
F3D J033850.24-353517.31	03h38m50.24s	-35d35m17.31s	28.32	3.7	-28.6	PN
F3D J033853.51-353516.34	03h38m53.51s	-35d35m16.34s	27.62	7.0	3.7	PN
F3D J033850.08-353515.62	03h38m50.08s	-35d35m15.62s	28.21	4.4	-0.9	PN
F3D J033851.25-353515.22	03h38m51.25s	-35d35m15.22s	28.41	3.0	-73.7	PN
F3D J033852.35-353515.09	03h38m52.35s	-35d35m15.09s	27.91	4.7	45.6	PN
F3D J033849.73-353514.89	03h38m49.73s	-35d35m14.89s	28.39	3.9	99.7	PN
F3D J033852.13-353514.09	03h38m52.13s	-35d35m14.09s	27.61	6.5	-103.6	PN
F3D J033849.32-353514.02	03h38m49.32s	-35d35m14.02s	28.2	5.1	-99.0	PN
F3D J033850.39-353512.70	03h38m50.39s	-35d35m12.70s	27.49	8.3	65.5	PN
F3D J033852.70-353508.44	03h38m52.70s	-35d35m08.44s	27.54	7.9	-149.3	PN

Table 5. FCC 219 - Table 2 continues

Source ID	RA (J2000)	Dec (J2000)	m_{5007}	A/rN	LOSV km/s^{-1}	Identifier
F3D J033852.88-353508.11	03h38m52.88s	-35d35m08.11s	28.28	4.2	162.1	PN
F3D J033850.64-353507.97	03h38m50.64s	-35d35m07.97s	28.0	5.6	-252.9	PN
F3D J033851.24-353507.59	03h38m51.24s	-35d35m07.59s	28.55	3.2	160.2	PN
F3D J033850.94-353506.70	03h38m50.94s	-35d35m06.70s	27.35	9.8	-60.7	PN
F3D J033850.08-353505.48	03h38m50.08s	-35d35m05.48s	27.39	10.9	-264.0	PN
F3D J033853.96-353505.28	03h38m53.96s	-35d35m05.28s	28.14	5.2	143.3	PN
F3D J033853.81-353502.60	03h38m53.81s	-35d35m02.60s	28.23	4.4	-166.7	PN
F3D J033851.63-353502.57	03h38m51.63s	-35d35m02.57s	28.58	3.3	-76.1	PN
F3D J033849.53-353502.86	03h38m49.53s	-35d35m02.86s	27.39	11.7	110.8	PN
F3D J033850.58-353449.83	03h38m50.58s	-35d34m49.83s	28.08	6.0	-5.0	PN
F3D J033852.03-353448.52	03h38m52.03s	-35d34m48.52s	28.11	5.6	62.0	PN
F3D J033851.22-353445.96	03h38m51.22s	-35d34m45.96s	28.47	4.3	-91.4	PN
F3D J033850.91-353443.34	03h38m50.91s	-35d34m43.34s	28.07	6.2	-213.1	PN